

**OPTICAL SCATTERING AND SENSITIZATION OF TiO₂ NANOWIRES COATED
WITH PBS SHELL**

by

Jianan Xiao

B.S. in Material Science & Engineering, Jiangsu University of Science and Technology, 2012

Submitted to the Graduate Faculty of
Swanson School of Engineering in partial fulfillment
of the requirements for the degree of
Master of Science

University of Pittsburgh

2014

UNIVERSITY OF PITTSBURGH
SWANSON SCHOOL OF ENGINEERING

This thesis was presented

by

Jianan Xiao

It was defended on

November 26, 2014

and approved by

Jung-Kun Lee, PhD, Associate Professor,

Department of Mechanical Engineering and Material Science

Qing-Ming Wang, PhD, Professor,

Department of Mechanical Engineering and Material Science

Guofeng Wang, PhD, Assistant Professor,

Department of Mechanical Engineering and Material Science

Thesis Advisor: Jung-Kun Lee, Associate Professor,

Department of Mechanical Engineering and Material Science

Copyright © by Jianan Xiao

2014

OPTICAL SCATTERING AND SENSITIZATION OF TiO₂ NANOWIRES COATED WITH PBS SHELL

Jianan Xiao, MS

University of Pittsburgh, 2014

Light absorption and transmittance by an array of TiO₂ nanorods with different lengths 200-1000nm and diameters 12–22 nm were theoretically studied using the electromagnetic computational technique, finite-difference time domain (FDTD). Then the nanowires were fabricated via the hydrothermal methods and their optical properties were experimentally measured and compared with the theoretical results. The nanowire length and diameter were found to be major parameters in modifying the intensity and the wavelength of the scattered radiation, respectively. In addition, light absorbing behavior of a very thin semiconductor layer (PbS) coated on the surface of highly ordered TiO₂ nanorod arrays was simulated. The numerical simulation model is comprised of nanorod arrays grown on a transparent conducting film of glass substrates under front-side illumination. In the FDTD analysis, a transverse electromagnetic (TEM) wave is incident onto PbS or TiO₂ first and passing through the barrier layer.

Two monitor planes placed above the electromagnetic source and below nanorod arrays detect the intensity of both the incident wave and the reflected/scattered wave from the TiO₂ nanorod structure. The absorption and transmission spectra are determined in the wavelength range 300–700nm as a function of nanorod length, nanorod diameter, and interface barrier layer thickness. In a part of simulation models, PbS shell with the thickness of 10 nm was added on the surface of the nanorod arrays. Results of the electrodynamic simulations were experimentally

verified. A significant increase in the light absorption by the PbS-coated nanorods was observed by increasing the nanorod length and decreasing the nanorod diameter. Changes in the barrier layer thickness between the nanorod and the substrate had a negligible effect on the scattering and absorbance spectra.

TABLE OF CONTENTS

PREFACE.....	XI
1.0 INTRODUCTION.....	1
2.0 LITERATURE REVIEW.....	5
2.1 OPTICAL BACKGROUND.....	5
2.1.1 Light Absorption and optical loss	5
2.1.2 Basic Operation Principles of Solar Cells.....	12
2.2 WIDE BANDGAP SEMICONDUCTOR TITANIA DIOXIDE	16
2.2.1 Structure of TiO₂	16
2.2.2 Growth Mechanism of 1D TiO₂ Nanostructure (Oriented Attachment)..	18
2.2.3 Synthesis of 1D TiO₂ Nanomaterials (Solution –based and Microwave-assisted Methods)	22
2.2.4 Carrier Transport in Metal Oxide Films	24
2.2.4.1 Mechanism of photoinduced carrier transport	24
2.2.4.2 Diffusion Length.....	27
2.2.4.3 One- Dimensional (1-D) transport architectures	28
2.3 COLLOIDAL QUANTUM DOTS.....	30

2.3.1	Introduction	30
2.3.2	Basics of Colloidal Synthesis: Nucleation and Growth	30
2.3.3	Electronic Structure and Shell Filling of Semiconductor Nanocrystals ...	34
2.3.4	Multiple Exciton Generation in Semiconductor Quantum Dots.....	36
2.4	DEVICE APPLICATION AND COMPARISON	39
2.5	FINITE DIFFERENCE TIME-DOMIAN (FDTD) TECHNIQUE	42
2.5.1	Introduction	42
2.5.2	FDTD modeling of solar energy absorption in PbS sensitized TiO ₂ nanorods.....	45
3.0	METHODOLOGY.....	48
3.1	TiO ₂ NANOWIRE FABRICATION AND CHARACTERIZATION	48
3.2	FDTD SIMUATION AND MODELING.....	49
4.0	RESULTS AND ANALYSIS.....	56
4.1	RESULTS FOR COMPUTATIONAL MODEL	56
4.1.1	Simulation Modeling	56
4.1.2	Data Analysis.....	58
4.2	EXPERIMENT	66
5.0	CONCLUSION.....	68
	REFERENCES.....	69

LIST OF FIGURES

Figure 1. Optical absorption generates electron-hole pairs ³⁶	6
Figure 2. Absorption coefficient for different materials ³⁷	8
Figure 3. density of states and absorption coefficient.....	9
Figure 4. (a) p-n junction solar cell structure (b) Current-voltage characteristics of a solar cell ³⁸	13
Figure 5. Lattice Structure of TiO ₂ ⁴²	18
Figure 6. Anatase tetragonal {101} bi-pyramid truncated by (001) and (001) facets ⁴²	20
Figure 7(a) Schematic model illustrating the oriented aggregation mechanism (b) TEM image of a crystal dimer formed by oriented attachment mechanism ⁴²	21
Figure 8. Comparison for electron and hole pathways for different structures ¹⁰¹	26
Figure 9. Examples of synthesized metal and metal alloy nanoparticles ³⁸	33
Figure 10. (a) Size-dependent electronic structure of individual semiconductor nanocrystals (b) Electronic states in the valence and conduction bands corresponding to the atomic-like S, P and D orbitals (c) The electrochemical potentials for sequential additions of electrons to typical semiconductor nanocrystals ³⁸	36
Figure 11. Multiple electron-hole pair (exciton) generation (MEG) in quantum dots ²⁰⁶	39
Figure 12. Comparison of three CQD photovoltaic architectures ²¹⁰	40

Figure 13. Yee Cell ²¹²	45
Figure 14. light and carrier interactions between p-n junction (a) planar junction (b) radial junction	46
Figure 15. A schematic of the titania nanotube quantum dots-sensitized solar cell	49
Figure 16. A schematic for two-dimensional FDTD model	51
Figure 17. Optical constant spectra of titania-n	53
Figure 18. Optical constant spectra of titania-k	53
Figure 19. Optical constant spectra of PbS-n	54
Figure 20. Optical constant spectra of PbS-k	54
Figure 21. Simulation window for the titania arrays	57
Figure 22. Simulation window for the titania based quantum dots solar cell	58
Figure 23. The comparison transmission data between experiment and FDTD simulation	59
Figure 24. FDTD simulated transmission of titania-based solar cell of 1000 and 200nm in length with and without PbS coating.	60
Figure 25. FDTD simulated absorption of titania-based solar cell of 1000 and 200nm in length with and without PbS coating.	61
Figure 26. FDTD simulated transmission of titania- based quantum-dots solar cell as a function of nanowire length	62
Figure 27. FDTD simulated absorption of titania- based quantum-dots solar cell as a function of nanowire length	62
Figure 28. FDTD simulated transmission of titania- based quantum-dots solar cell as a function of radius.	63
Figure 29. FDTD simulated absorption of titania- based quantum-dots solar cell as a function of radius	64

Figure 30. FDTD simulated transmission of titania- based quantum-dots solar cell as a function of barrier layer..... 65

Figure 31. FDTD simulated absorption of titania- based quantum-dots solar cell as a function of pore size (radius)..... 65

Figure 32. SEM cross section view for the 2 μm TiO_2 nanowire 66

Figure 33. SEM top view for the 2 μm TiO_2 nanowire 67

PREFACE

I thank my advisor, Dr. Jung-kun Lee, for helping me prepare for independent scientific research. He provides the Lab equipment and software license so that I can do this project. Moreover, I thank the members of his group, especially, Salim Caliskan, Po-shun Huang, Ziyue Xiong, and Zhimin Sun. for giving a lot of help in my thesis.

I express my gratitude to my thesis committee members, Dr. Jung-kun Lee, Dr. Qing-Ming Wang, and Dr. Guofeng Wang, for their attention and patience.

Finally, I have to express my extreme appreciation towards my parents for encouragement and support during my master study.

1.0 INTRODUCTION

One of the greatest challenges facing mankind in the 21st century is energy. In order to meet the increasing energy demand in the near future, we will be forced to seek environmentally clean alternative energy resources.¹ Photovoltaic (PV) cells have been highly valued among all potential technologies.²⁻³ Silicon photovoltaics have been developed to convert sunlight into electricity at relatively high efficiencies and provide the most feasible carbon-neutral route to displacing terawatts nonrenewable power consumed worldwide.⁴ However, large-scale implementation is currently not economically feasible because of the high cost. One of the primary costs for silicon photovoltaic cells is the starting silicon wafer, which requires extensive purification to maintain reasonable performance.⁵⁻⁷ Also, the theoretical power conversion efficiency limit for a typical single-junction crystalline silicon PV cell detailed by Shockley and Queisser is ~33% under the standard AM1.5 solar spectrum. Therefore, reducing the quality and quantity of semiconductors will help drive large-scale implementation of PVs. Using PVs with nanostructured radial p-n junctions may solve both of these problems simultaneously. There are several types of core inorganic materials for the photoactive component of PVs. The application of semiconductor nanostructures within devices is one of the major goals of current nanotechnology. For example, semiconductor nanorods have been attracting much attention due

to their unique electrical, optoelectronic properties that, together with their low cost and ease of preparation, make them potentially useful in PV applications.

Nanowire/nanorods have demonstrated high diffusion coefficient of carriers due to their unique one-dimensional (1D) structure. When the nanoparticle-based photoanode solar cell is substituted with the nanorods-based photoanode, it is expected that the nanorods provide a ballistic pathway to the carriers and enhance the carrier transport. Moreover, the nanorods and nanowires scatter incoming light and increase light propagation path in the photoelectrode, which reduces the portion of light transmitting the photoelectrode. Therefore, nanorods and nanowires point a way toward to PVs with high solar-electricity conversion efficiency and low cost.⁸⁻¹⁰

The nature of electron transport in oxide nanorods films in the nanostructured electrode of PEC cells is fairly well understood. Time-resolved photocurrent and photovoltage measurements and modeling studies indicate that electron transport in wet, illuminated nanoparticle networks proceeds by a trap-limited diffusion process, in which photon-generated electrons repeatedly interact with a distribution of traps as they undertake a random walk through the film. Drift transport of electrons, a vital mechanism in most photovoltaic cells, is not observed in PEC-type PVs. Instead, photogenerated electrons couples with ions in the electrolyte that screen macroscopic electric fields. This strong attraction between ions and electrons effectively render them neutral carriers. Ambipolar diffusion in crystalline nanorods and nanowires is expected to be several orders of magnitude faster than in a random network of the nanoparticles. Using a sufficiently dense array of long, thin nanowires is possible to increase the

absorption of light while simultaneously maintaining very efficient carrier collection. Moreover, the rapid transport provided by a nanowire anode would be particularly favorable for cell designs that use non-standard electrolytes, such as polymer gels or solid inorganic phases, in which recombination rates are high compared with the liquid electrolyte. In contrast to the carrier transport, the light scattering by the nanorods and nanowires is not well known. Since the diameter and length of the nanorods are 50 - 500 nm and 500 nm - 20 μm , Mie scattering is dominant over Rayleigh scattering in the nanorod arrays. As the length of the nanorods increases, the nanorod array scatters travelling light successively at different parts of the nanorod and the transmittance of the incident light decreases dramatically. However, multiple light scattering occurring in the nanorod array is not easily calculated by the analytic approach, which requires the implementation of the numerical approach to the simulation of the light absorption.

Appropriate electronic band structure and excellent surface activity of TiO_2 are very beneficial to the applications of hydrogen production, photovoltaic, photocatalysts, lithium-ion batteries, fuel cells, gas sensors, detoxification, and supercapacitors.¹¹⁻²¹ For example, solar cells sensitized by dyes, quantum dots (QDs) and inorganic-organic hybrid semiconductor have all been built on TiO_2 -based electrodes. They offer a higher power conversion efficiency and more stable performance than other oxide material based electrodes.^{18,22-25} The structure, processing, property, and application of TiO_2 -related materials have been extensively studied since the photocatalytic effect of TiO_2 was first observed in 1970s.²⁶⁻³² Most TiO_2 applications were based on its nanoscale morphologies, particularly the form of nanoparticles which exhibited a high surface-to-volume ratio and a quantum confinement effect.³³⁻³⁵ Nevertheless, although TiO_2

possess such promising potentials, the wide bandgap (~ 3.2 eV) and polycrystalline nature of TiO₂ nanoparticle electrode of TiO₂ still need to be addressed for its contemporary applications in energy harvesting/storage and environmental cleaning. Further improvement on the performance of TiO₂-based devices and systems will rely on the development of appropriate nanostructures with well-engineered composition and crystallography, which will allow for visible light absorption and less carrier trapping.

Finite-difference time-domain (FDTD) invented by Professor Kane Yee, is a popular computational technique for simulating the propagation of electromagnetic waves through inhomogeneous objects ranging from aircraft to human tissue. With FDTD the space containing the object of interest is divided into two or three-dimensional grids. Based on the Maxwell's equations, the FDTD operator updates the electric and magnetic fields in all grids at increasing time steps, allowing determination of the electromagnetic wave in real time. Here, the purpose of this work is to study the propagation of light through PbS-sensitized TiO₂ nanorod arrays to explore the light scattering by the nanorod and the light absorption by PbS shell. As the nanorod length increases, the amount of the transmitted light is significantly reduced and the theoretical efficiency of the solar cell is dramatically increased. Results of this research provide a guideline to simulate the electrodynamics of the sensitized nanorod and design the optimum dimension and architecture of the nanorod based PVs.

2.0 LITERATURE REVIEW

2.1 OPTICAL BACKGROUND

2.1.1 Light Absorption and optical loss

Photons incident on the surface of a material will be either reflected from the top surface, will be absorbed in the material or, failing either of the above two processes, will be transmitted through the material. Carrier generation is a process due to light absorption occurs by light injecting the semiconductor if the photon energy is large enough to raise an electron from the valence band into an empty conduction band state, thereby generating one electron-hole pair. In order to finish the process, the photon energy is required to be larger than the bandgap energy. A photon of energy $h\nu$ greater than bandgap E_g can be absorbed in a semiconductor, resulting in the excitation of an electron from the valence band to the conduction band. The energy of the incoming photons is used to raise an electron from a lower energy level to a higher energy level, as illustrate as Figure 1. The average energy of electrons in the conduction band is $\frac{3}{2}kT$ above the E_c (average kinetic energy is $\frac{3}{2}kT$), which illustrates that the electrons are very close to the

conduction band energy. If the photon energy is much large than the bandgap energy E_g , then the excited electron is not near E_c and has to lose the extra energy $h\nu - E_g$ to reach the thermal equilibrium. The excess energy is lost to lattice vibration as heat as the electron is scattered from one atomic vibration to another. This process is called thermalization. On the other hand, the photon energy is less than the bandgap energy, the photon will not be absorbed and we can say that the semiconductor is transparent to wavelength longer than $\frac{hc}{E_g}$ provided that there is no energy state in the bandgap. There would be a reflection occurring at the air /semiconductor surface due to the change in the refractive index.

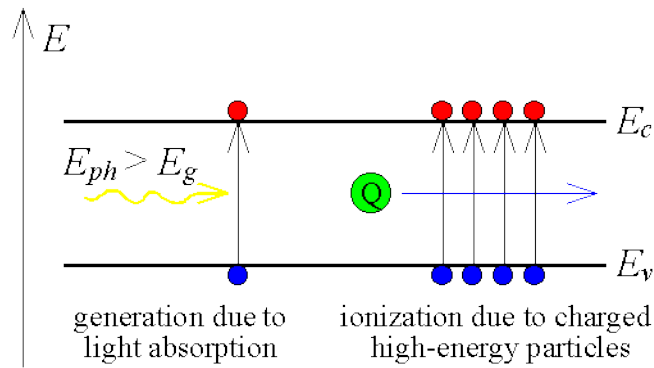


Figure 1. Optical absorption generates electron-hole pairs³⁶

It is assumed if I_0 is the intensity of a beam of photons incident on a semiconductor material, the unit of which is energy per unit area per unit time. Γ_{ph} is the photon flux, then,

$$I_0 = h\nu\Gamma_{ph} \quad (1)$$

The absorption of photons requires the excitation procedure of valence band electrons, and there are only some of them with the appropriate energy per unit volume. As a result, thickness of the injected semiconductor is mainly a key factor for the light absorption. $I(x)$ is the light intensity at x and δI is the change of light intensity in the small elemental volume of thickness δx at x due to the light absorption. Then δI will depend on the number of photons arriving at the this volume $I(x)$ and the thickness δx . Thus,

$$\delta I = -\alpha I \delta x \quad (2)$$

α is proportional constant, which is determined by the photon energy. In other word, it refers to the wavelength. The negative value of the constant indicates that the change of the light intensity is decreasing. Additionally, the constant is defined as the absorption coefficient of the semiconductor. The absorption coefficient α means the distance into a material light of a particular wavelength can penetrate before it is absorbed. Specifically it is defined by,

$$\alpha = -\frac{\delta I}{I \delta x} \quad (3)$$

In a material with a low absorption coefficient means the poor absorption for the certain range of the wavelength, and if the material is ultrathin, it will become relatively transparent to that wavelength range. Normally semiconductor materials have a sharp edge for their absorption coefficient, since light which has energy below the band gap does not have enough energy to bring an electron from the valence band to the conduction band. As a result, this light is not absorbed by this semiconductor type. The absorption coefficient for several semiconductor materials is shown in Figure 2.

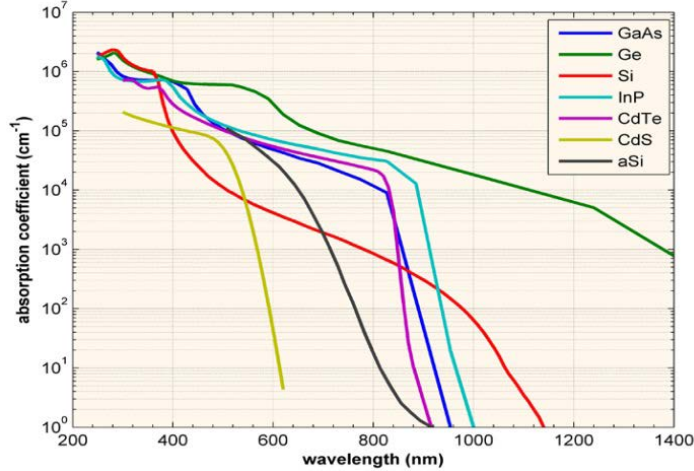


Figure 2. Absorption coefficient for different materials³⁷

The above graph shows that even for those photons which have the energy large than the band gap, the absorption coefficient is not kept as constant, but it still depends strongly on change of wavelength. The probability of absorbing a photon is determined by the likelihood of having a photon and an electron interact as to move from one energy band to another. For those photons which have the photo energy close to that of the band gap, the absorption is relatively low due to that case only those electrons directly at the valence band edge can interact with the photon to be absorbed. With the photon energy increasing, not only the electrons already having energy close to that of the band gap can interact with the photon. Also, a certain number of electrons can response with the photon and result in the photon being absorbed.

Density of states (g_E) is defined as the number of states per unit energy per unit volume. On the assumption of that Valence Band (VB) states are filled and the Conduction Band (CB) states are empty. Normally the number of the electrons in the CB is less than its states in this band. It seems that absorption process caused by the light injection increases when there are more VB states

available in a result more electrons are excited. The corresponding CB states are also required for electrons to find their empty states to fill. Thus, the possibility of photon could be absorbed depends on both the density states of the VB and the CB density states. For photons of the energy $h\nu_A = E_g$, the absorption can only occur from E_v to E_c where the density of states of VB and CB are low and thus the absorption coefficient is small, which is illustrated as A in the Figure 3. For Photon energies $h\nu_B$, it can bring electrons from the middle region of the VB to the middle of the CB, so the density of states are large and α is also large indicated by B in the figure. For the C case, because the energy becomes too high and the density of states in the valence band reduces, as a result, the absorption is less.

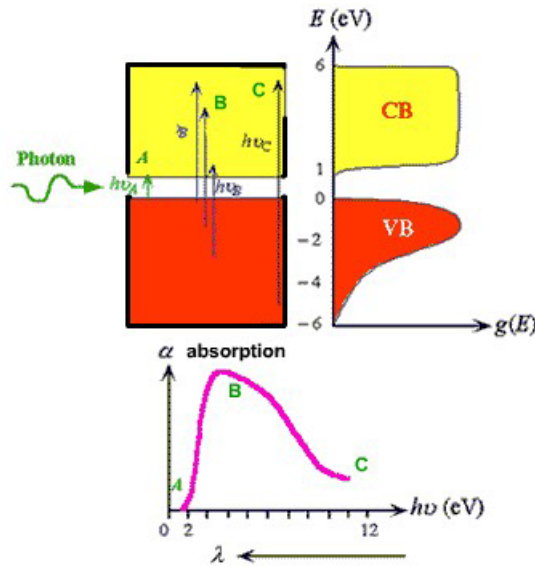


Figure 3. Density of states and absorption coefficient

In addition, the absorption process has to satisfy the conservation of momentum and quantum mechanism transition rules. The rules define that certain transition from the CB to VB

will have the priority than others. For example, GaAs is a direct bandgap semiconductor, so photon absorption can lead directly to the excitation of an electron from the CB to VB for photon energies just above the bandgap energy. Oppositely, the Si is the indirect bandgap semiconductor. Thus it could not occur in silicon that the direct recombination of electrons and holes, the electron excitation from states near E_v to states near the E_c must be accompanied by the emission or absorption of lattice vibration, and hence the light absorption is less efficient than other direct bandgap semiconductors. Absorption of semiconductors in real solar cells can be improved by eliminating several extrinsic limitations. These include losses due to reflection, contact shadowing, series resistance, incomplete collection of photogenerated carriers, absorption in inactive window layers, nonradiative recombination, and above ambient cell temperature. One of the ways for increasing the efficiency of solar cells is reducing the optical losses at the interaction of light with a semiconductor material. For example, decreasing reflection, or increasing the path length of the radiation in the structure, consequently increase the light absorption. Another way is creation of the cell structure that absorbs light most effectively from a standpoint of photoelectromotive force, which is caused by spatial separation of the light-generated charge carriers by the electric field of the p–n junction. Only carriers generated in the space–charge (depletion) region and adjacent areas determined by the diffusion length of the minority carriers are separated.

Even if these losses are completely eliminated, there remain two intrinsic losses which then determine the efficiencies of ideal solar cells. The first are losses because of the inability of a single energy gap solar cell to properly match the broad solar spectrum. A key factor in

determining if a photon is absorbed or transmitted is the energy of the photon. Therefore, only if the photon has enough energy will the electron be excited into the conduction band from the valence band. Photons falling onto a semiconductor material can be divided into three groups based on their energy compared to that of the semiconductor band gap: 1) $E_{ph} < E_g$ where photons with energy E_{ph} less than the band gap energy E_g interact only weakly with the semiconductor, passing through it as if it were transparent; 2) $E_{ph} = E_g$ where photons have just enough energy to create an electron hole pairs without energy loss; 3) $E_{ph} > E_g$ where photons with energy much greater than the band gap are strongly absorbed. However, when $E_{ph} > E_g$, photon energy greater than the band gap is wasted as electrons quickly thermalize back down to the conduction band edges for photovoltaic applications. The second intrinsic loss is due to radiative recombination. All solar cells absorb sunlight and consequently radiate light. The rate of radiative emission increases exponentially with the bias energy eV where, for an ideal cell, V is the voltage developed across the load. The radiative current subtracts from the current delivered to the load by the cell. When V is adjusted to deliver maximum power, eV is about 0.4 to 0.5 electron volts less than E_g . This is an intrinsic loss because the radiative current of an ideal cell as a function of V is directly determined by the laws of thermodynamics and the statistical mechanical formula for the entropy of radiation.

2.1.2 Basic Operation Principles of Solar Cells

A photovoltaic solar cell is an electronic device which directly converts sunlight into electricity. Light shining on the solar cell produces both a current and a voltage to generate electric power. This process requires firstly, a material in which the absorption of light raises an electron to a higher energy state, and secondly, the movement of this higher energy electron from the solar cell into an external circuit. The electron then dissipates its energy in the external circuit and returns to the solar cell. A variety of materials and processes can potentially satisfy the requirements for photovoltaic energy conversion. The common examples include a p-n junction, a network of donor-acceptor pairs, Schottky barrier, or semiconductor-liquid interface. Operation of a solar cell can be indicated by its I-V characteristics as shown in Figure 4. In the dark, The I-V curve of a solar cell is the superposition of the I-V curve of the solar cell diode in the dark with the light-generated current, typically for a p-n or Schottky junction. There is very little dark current flowing under reverse bias, and there is an abrupt current increase when the device is biased in the forward direction. Under illumination, the I-V curve of a solar cell exhibits a vertical shift caused by light-induced current generation in Figure 4. Device produces power only when operating in the forth quadrant, that is, under the condition when biased in the forward direction and applied voltage is between zero and open circuit voltage V_{oc} . Many performance parameters for the cell can be determined from the I-V scan, as described below.

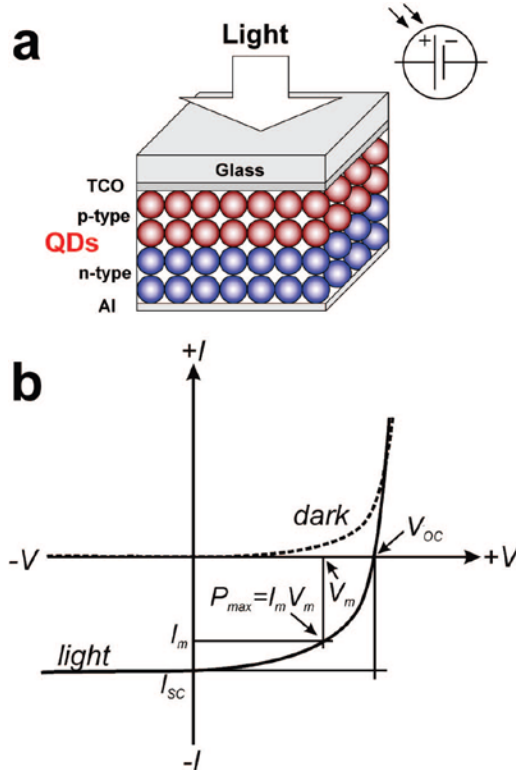


Figure 4. (a) p-n junction solar cell structure (b) Current-voltage characteristics of a solar cell³⁸

Open-circuit voltage V_{oc} is the maximum voltage available from a solar cell when the value of current is zero. The open-circuit voltage corresponds to the amount of forward bias on the solar cell due to the bias of the solar cell junction with the light-generated current. Under these conditions, there is no electric current flowing through the external circuit. The open-circuit voltage is the maximum possible voltage that can be generated by a solar cell. The structure and energy diagram of the device has the key effect on this parameter. Because the mechanism of the photoconversion is various in different solar cells, different effects can contribute to V_{oc} . Specifically, the built-in potential associated with p-n junction determines V_{oc} of conventional solar cells with a planar junction. V_{oc} can be also caused by the difference

in the different work functions of two metals, which contacts in a simple metal-semiconductor-metal structure, also it could be created by the difference between the work function of the metal contact and the semiconductor quasi-Fermi levels in Schottky solar cells. Some factors, such as morphological characteristics, chemical processing, and trap states formed at junction interfaces, could also change the value of V_{oc} .

Short-circuit current is the parameter determined by the product of the charge carrier density n under illumination, carrier mobility μ , and the electric field E acting on the carriers:

$$I_{sc} = en\mu E \quad (4)$$

I_{sc} the short-circuit current is due to the generation and collection of light-generated carriers. For an ideal solar cell at most moderate resistive loss mechanisms, the short-circuit current and the light-generated current are identical. Therefore, the short-circuit current is the largest current which may be drawn from the solar cell. The short-circuit current depends on a number of factors, such as, the area of the solar cell, the number of photons, the spectrum of the injected sunlight, the optical properties of the solar cell materials, and also the collection probability of the PV cells.

The external quantum efficiency(IPCE), can be determined as:

$$IPCE(\lambda) = \frac{1240}{\lambda} \frac{I_{sc}}{P_{in}} \quad (5)$$

where P_{in} is an incident power at wavelength λ . If one electron-hole pair is created and at the same time separated per every absorbed photon, then the ultimate ICPE is calculated as 100%. Generally, photogenerated carriers is determined by the multiple product of $\mu\tau$, in which μ is the

mobility of charges, and τ is the carrier lifetime. In order to get ideal efficiency, the carrier lifetime has to be large enough to enable carrier separation before their recombination. Additionally, the ICPE parameter can be larger than 100%, which means PV solar cells have the ability to generate more than one electron and hole pairs per absorbed photon, for example, via impact ionization or carrier multiple exciton processes.

The fill factor (FF) determines the quality of voltage-current characteristics. It is defined as the ratio of the maximum power P_{\max} under matched load conditions to the product of the open circuit voltage V_{oc} and the shortcircuit current I_{sc} :

$$FF = \frac{I_m V_m}{I_{sc} V_{oc}} \quad (6)$$

The efficiency of a solar cell is determined as the fraction of incident power which is converted to electricity, which is defined as the ratio of the maximum power from the solar cell to the product of short circuit current and open circuit voltage. Typically, shunt resistances inside a solar cell account for a decrease in the fill factor. Power conversion efficiency (η) by definition is the maximum fraction of the input optical power converted into the electrical power:

$$\eta = \frac{P_{max}}{P_{in}} = FF \frac{I_{oc} V_{sc}}{P_{in}} \quad (7)$$

This source which called AM1.5 (air mass of 1.5) was characterized by the power density of $\sim 1000 \text{ W/m}^2$ with the spectral intensity distribution matching that of sunlight at the earth's surface at an incident angle of 48.2° . And it is often be used both in experiment and simulation input optical power to compare different solar cells.

2.2 WIDE BANDGAP SEMICONDUCTOR TITANIA DIOXIDE

2.2.1 Structure of TiO₂

Understanding the basic crystal structure of TiO₂ NWs is the critical step toward rational experimental design for synthesizing and simulation modeling. As the development of the advanced electron microscopy techniques, the atomic structures of different TiO₂ phases could be directly observed. Basically TiO₂ naturally exhibits four different types of crystal structures, specifically, rutile, anatase, brookite, and TiO₂(B).³⁹ Moreover, several metastable crystal structure, such as TiO₂ (H), TiO₂ II, and perovskite, have also been mentioned in some research studies. Different phases have different properties, thus they demand different conditions to form desired morphologies and eventually exhibit different material performance. In a sum, rutile is the most stable phase, while the anatase, brookite, and TiO₂ (B) are relatively metastable. However, they will transform into rutile under the high temperature experiment conditions. As expected, this phase stability is also related with the TiO₂ nanomaterial fabrication. Anatase phased nanomaterials were normally produced in solution-based method, or it might also be found in low-temperature vapor deposition systems. In the contrast, annealing and under high temperature deposition often lead to rutile phase TiO₂ nanostructures. Additionally, Brookite and TiO₂ (B) phases of the TiO₂ nanostructures which normally synthesized under the solution-based experiment method were less common than the other two. Other metastable phases have to be

fabricated using special types precursors and under restrict experiment conditions which were very rarely observed as a normal stable nanomaterial phase.

Figure 5 shows the schematic of the four common TiO₂ phase's crystal structures. In the figure, the Ti-O octahedrons fundamental building block could be seen in all four types. These four phases have different crystal symmetry and their nanostructures always exhibit different growth behaviors and preferred morphologies. And it will be illustrated in details, Rutile TiO₂ has a tetragonal structure with $a = 0.459$ nm and $c = 0.296$ nm.⁴⁰ {011} and {100} are the two surface families with the lowest energy and thus the thermodynamically preferred equilibrium morphology of rutile TiO₂ is a trunked octahedron. Rutile is also the mostly common morphology from synthetic rutile TiO₂ powders. The anatase phase is tetragonal same as the rutile phase, but what is different is that it has a longer c -axis (0.951 nm) with comparison to the a -axis (0.379 nm). Similarly, the TiO₂ anatase phase also has the same lowest energy surfaces with rutile phase. As a result, trunked octahedron morphology is preferred. Brookite is orthorhombic crystal structure and has a large unit cell consisting of 8 TiO₂ groups. TiO₂ (B) also has a large unit cell with a more open crystal structure compared to other ones. As shown in the Figure 5, it is monoclinic with a particularly long a -axis (1.216 nm).⁴¹

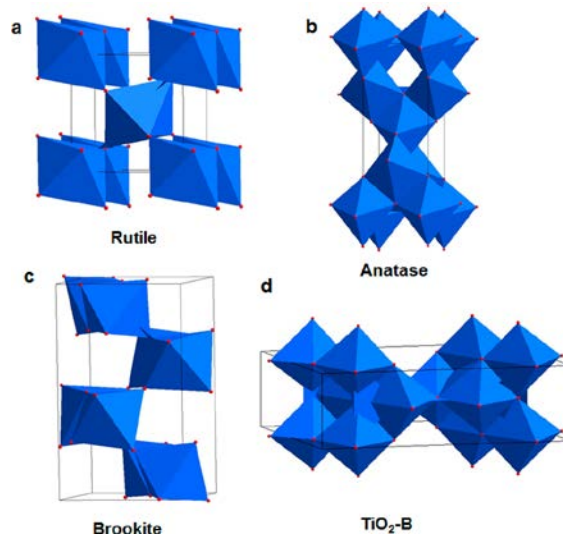


Figure 5. Lattice Structure of TiO₂⁴²

2.2.2 Growth Mechanism of 1D TiO₂ Nanostructure (Oriented Attachment)

In order to achieve 1D morphologies, such as nanowires and nanorods, it is very important to achieve one rapid growth direction during the development of nanocrystals. For certain types of crystals, this requirement is easier to be obtained due to the strong anisotropic property of their crystal structures. For example, wurtzite metal oxide crystals naturally have selective rapid growth along the [0001] direction, and thus nanowire is one of the preferred morphologies during self-assembly growth. However, for some other crystals, such as TiO₂, such anisotropy is less obvious, and normally they demand additional kinetics to realize the 1D morphologies. There are many methods to achieve this property, such as applying catalysts to induce a rapid precipitation interface, introducing some crystal defects, like dislocations (screw, twin, etc.), which is used to increase the growth rate along the crystal defects direction. Also surface

functionalization can be used to increase the deposition difference among different facets in crystal structures, and it could also be obtained via adding the building block concentrations to accentuate the assembly rate differences along different crystal facets. Many articles has been well reported both of the experiment and results details to illustrate this methods .⁴³⁻⁴⁶ Among these approaches, some of them have been successfully studied and used to fabricate the TiO₂ 1D nanostructures.⁴⁷⁻⁵¹

Previously, Ostwald ripening was assumed to be a major explanation regarding mechanism for the growth of large crystals from massive small particles in TiO₂ nutrient solution. Penn et al. clearly reported that the formation of some 1D TiO₂ nanostructures in solution followed the oriented attachment mechanism.⁵² Oriented attachment is the assembling procedure of TiO₂ nanocrystals based on their crystallographic orientations and gathering these nanocrystals into a single crystalline 1D nanostructure. More specifically, the driving force of an oriented attachment growth is the removal of certain type crystal facets with a high surface energy to decrease the surface energy. Barnard et al. have successfully proved it via calculating the density function theory (DFT). Seen as a thermodynamically stable anatase (as it is the most observed early stage phase in hydrothermal growth) TiO₂ is shown in Figure 6, the prime side facets are (101) facets and the top and bottom facets are (001) and (00 $\bar{1}$), respectively.⁵³

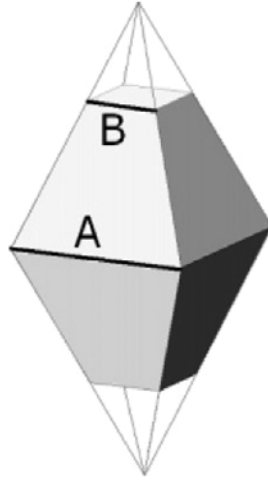


Figure 6. Anatase tetragonal {101} bi-pyramid truncated by (001) and (00 $\bar{1}$) facets⁴²

This structural type of the crystals is exactly same with what has been proved by Penn et al. and Shi et al. through the advanced material techniques (transmission electron microscopy (TEM)).^{54,55} As mentioned in articles with the DFT calculation by Penn et al., surface free energy of the (001) surface of anatase TiO₂ is 0.51 J/m²; 0.39 J/m² for the (100) surface and 0.35 J/m² for the (101) surface. They assumed that during the initial nucleation step, when the number of TiO₂ nanocrystals reaches a critical value, the titania nanocrystals diffuse and then gather together through the (001) facets direction to form a 1-dimension (1D) structure without coarsening by the Ostwald ripening process, which is illustrated in Figure 7.⁵⁶ It was seen that the curly region with a negative curvature was created by the attachment. They can be easily filled in the growth stage, which comes directly from the deposition of the molecular TiO₂ in the nutrient solution caused by the large surface free energy gain. Thus, the titania one dimension

nanostructure might not be seen to prove the original oriented attachment mechanism theory under a long growth time.

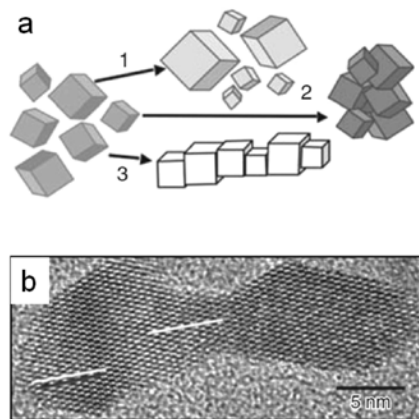


Figure 7(a) Schematic model illustrating the oriented aggregation mechanism (b) TEM image of a crystal dimer formed by oriented attachment mechanism⁴²

Many structure models were set up to illustrate and quantify the oriented attachment growth. For example, Penn come up with a simple molecular dimer formation model to quantify the process. The model put the assumption that the primary crystals were only regarded as molecules and only allowed the formation of so called dimers.⁵⁷ A dimer in this specific model means that an oriented aggregation which is composed of two primary TiO₂ crystals. The corresponding rate law for oriented attachment shown as

$$\frac{d[p - p]}{dt} = k[p]^2 \quad (8)$$

In this equation, k is a rate constant and P-P symbolizes two oriented attached particles. P-P dimerization requires the orientation rotation of individual particles and removal of the

intermediate solvent substances. For this model, the rate of oriented attachment process was second order-related to the concentration of primary particles which relatively consistent with the Derjaguin–Landau–Verwey–Overbeek (DLVO) theory, as both of the electrostatic repulsive and van der Waals attractive forces are taken into account. However, although the theory is relatively well established, one weakness of this model was that it only considered the presence of oriented aggregates with two primary particles. In order to complete the model and theory, Ribeiro et al. developed a stepwise kinetic model to explain the growth of one dimensional TiO₂ architecture, in which model primary particles were regarded as monomer and oriented aggregates as multimer.⁵⁸ From this model, viscosity and temperature of the solution are the main factors effecting on the kinetics of the oriented attachment growth, which instead is better consistent with experimental observations. Burrows et al. have further studied the oriented attachment kinetics quantification⁵⁹.

2.2.3 Synthesis of 1D TiO₂ Nanomaterials (Solution –based and Microwave-assisted Methods)

Many synthetic methods have been applied to the fabrication of 1D TiO₂ nanostructures from both bottom-up and top-down directions. Representative bottom-up approaches include a large variety of solution- and vapor-based growth methods.⁶⁰⁻⁶¹ Although bottom-up approaches remains as the major fabrication methods, several top-down procedures have also been explored for 1D TiO₂ growth, such as direct oxidation and electrochemical etching techniques.⁶²⁻⁶⁵

Specifically, the solution-based microwave-assisted synthetic methods will be illustrated in this section.

Solution-based growth techniques with its economic and simple processing characteristics provide several major advantages for nanomaterials synthesis.⁶⁶⁻⁷⁰ Many advanced nanomaterial systems that are currently commercially available are made via solution-based approaches, including colloidal nanoparticles and quantum dots. Solution-based syntheses were also the most popular approaches for growing TiO₂ nanostructures. During decades, titania nanowires were achieved with good 1D morphology and single crystallinity with the better studying for the kinetics in the nanowire growth. Nevertheless, morphology and physical property control are still the main challenges for the 1D TiO₂ nanostructures fabricated directly from solution.

The assistance of microwave in synthetic chemistry provides an alternative way for heating, which is considered to be simultaneous, selective, and volumetric with rapid heating rates.⁷¹⁻⁷³ Therefore, microwave-assisted synthesis heating can dramatically reduce the reaction time for synthesizing organic and inorganic materials mainly by kinetics control.⁷⁴⁻⁷⁶ The microwave irradiation provides a unique progressive heating pattern, which is particularly effective for fabricating nanomaterials.⁷⁷⁻⁷⁹ Additionally, Microwaves also support in nanomaterial shape control. The reason is that the microwave energy stimulates molecular dipolar polarization and ionic motion, rapid precursor dissolution and quicker reaction kinetics are induced, which results in high fluxes of nuclei with a large concentration gradient. Moreover, the microwave-induced dipole moment in primary nuclei building blocks facilitates interparticle

collision and anisotropic attachment along the polar direction. In a sum, this is the desired property for TiO₂ 1D nanomaterial growth.⁸⁰⁻⁸⁵

Microwave heating was mostly accompanied with hydrothermal processes to synthesize TiO₂ nanorods, where simple precursors and solvent systems will be applied.⁸⁶⁻⁸⁷ For instance, Jia et al. reported the synthesis of mesoporous anatase TiO₂ NRs through a microwave-assisted method. The large TiO₂ nanorods were accumulated in the form of gathering small necklace-shaped nanorods, which were assembled by spherical particles following the oriented attachment mechanism. The TiO₂ nanocrystal building blocks were formed by direct hydrolysis of TiCl₄ in diluted hydrochloric acid at room temperature. With the increasing temperature, the TiO₂ nanocrystals became more energetic and tend to aggregate into large particles in order to lower the overall energy of the system. The formation of a necklace-shaped nanorod would be preferred to minimize the high energy (001) surfaces to meet the thermodynamic equilibrium requirement, and thus the TiO₂ nanorod grew along the [001] direction. Long necklace-shaped nanorods would further produce a side by side assemble to get the thicker nanorods.

2.2.4 Carrier Transport in Metal Oxide Films

2.2.4.1 Mechanism of photoinduced carrier transport

In order to produce photocurrent in the PV solar cell, electrons carriers must transport through the film and reach a conductive junction after transferring through the metal oxide layer. However, in other way, these electrons may also take a part in some processes which may result

in decreasing the PV solar cell efficiency, for example, back transferring to the sensitizer, scavenging by the electrolyte or some other species around the electrolyte, or recombining with a hole. As is known, the faster an electron can be conducted through the transport layer, the higher the probability of collection at the photoanode.

Electron transport is explained classically by the Nernst-Planck equation: ⁸⁸⁻⁹³

$$J_e = C_e v - D_e \nabla C_e - \frac{nF}{RT} D_e C_e \nabla \varphi \quad (9)$$

The three terms on the right-hand-side of the equation represent convection, diffusion, and electrostatic transport respectively. C_e is the concentration of electrons, v is the flow velocity of the system, D_e is the diffusion constant of an electron, n is the number of charges, which in the case of an electron is -1, F is Faraday's constant, and φ is the electric potential. The concepts in the equation can still be applied to electrons within a photovoltaic cell, with some corrections, even previously is used for charged species in the E field. In this equation applied for the solar cells, the convection term is dropped due to the unmovable metal oxide transport layers in the PV solar cell. In single-crystal systems, band bending drives the charge transport, ⁹⁴⁻⁹⁶ as illustrated in Figure 8. Where band bending is resulted via the equilibration of Fermi levels across an interface caused by the buildup of a space charge layer.⁹⁷

In some cases such as doped silicon, electrons are forced by the bent Fermi level at the interface to move in a certain direction, helping to separate the electron and hole pairs. Electric fields in these systems are large enough compared with diffusion term in the Nernst-Planck equation especially in thin film types, thus, this diffusion term can also be dropped.⁹⁸⁻¹⁰⁰

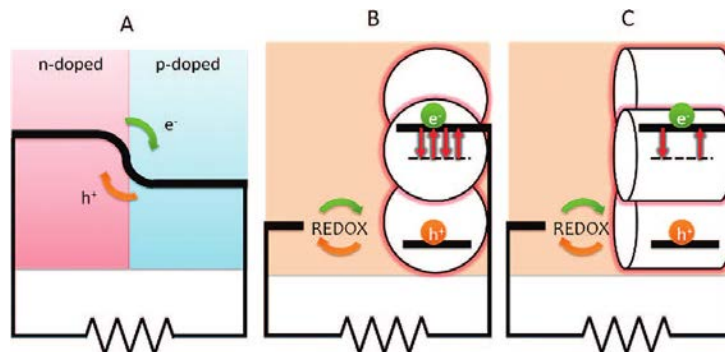


Figure 8. Comparison for electron and hole pathways for different structures¹⁰¹

In the systems of the nanoparticles, like dye or quantum dot sensitized solar cells, band bending no longer dominates in electron transport procedure. The magnitude of space charged layer for the nanoparticles are sever orders smaller than the layer in bulk systems, there is few electrostatic driving force existing.¹⁰¹⁻¹⁰⁵ Even if space charge layers were on the order of the nanoparticle radii, it has been shown that the electrolyte in contact with the porous film would deplete any space charge layer by eliminating excess charges.¹⁰⁶ Thus, diffusion becomes the key method of carriers transporting. In some models, a tiny gradient in Fermi levels between metal oxide nanoparticles is counted as a slight directionality force. However, several groups have shown that if the characteristic diffusion length (L_n) is larger than the film thickness, the efficiency of the cell will improves greatly,¹⁰⁷⁻¹⁰⁹ which indicates that diffusion is the only significant mechanism for carrier transport.

The modern description of electron transport through nanoparticles films, called the multiple trapping model, is well established till now.¹¹⁰⁻¹²⁰ This model states that photo-generated electrons will become trapped, subsequently detrap, and then move to a neighboring trap state on

their eventual transport path toward a conductive sink (Figure 8). Nonlinear intensity dependencies show that traps can become filled with carriers by increasing incident power density, allowing other electrons to flow freely in the conduction band of the nanoparticle film.¹²⁰⁻¹²⁷

2.2.4.2 Diffusion Length

Diffusion length is defined as $Ln = (D_0\tau_0)^{1/2}$, where D_0 is the diffusion constant of a free electron in the film and τ_0 is the characteristic lifetime of a free electron within that film.¹²⁸⁻¹³⁰ These intrinsic terms can be extracted using experimental techniques such as intensity modulation with intensity modulated photocurrent spectroscopy (IMPS), time resolved photocurrent response, or open circuit decay.¹³¹⁻¹³² However, the properties of free electrons cannot be directly measured due to traps in the system which cause seemingly slower mobilities than true free electrons.¹³³⁻¹³⁴ Instead, effective constants are measured. In some cases, it has been shown that the effective diffusion coefficients can be several orders of magnitude less than a free electron in bulk TiO_2 crystals, a discrepancy primarily due to the trapping events. To relate the free electron constants to effective constants, D_n and τ_n , Bisquert and Vikhrenko¹³³ developed a model for dye sensitized solar cells which relates both constants to the changes in population of the occupied traps, n_L , and changes to the electron population in the conduction band, n_c .

$$\tau_n = \left(\frac{\partial n_L}{\partial n_c}\right)\tau_0 \quad (10)$$

$$D_n = \left(\frac{\partial n_c}{\partial n_L}\right)D_0 \quad (11)$$

When combined to calculate the diffusion length, the two population rate terms cancel and the same diffusion length is determined. From this analysis, it was also shown that there is no theoretical Fermi level dependence on the diffusion length, which is also observed experimentally using steady state experiments, like IPCE.¹³⁴

Because there is no inherent directionality in electron transport, and as stated above, the small gradient in Fermi levels is negligible, diffusion through traditional nanoparticulate films is an inefficient mechanism for driving electrons to a conductive contact for photocurrent extraction. This mechanism creates a random walk process in which only a fraction of the excited charges are collected, especially with quantum dot sensitizers.¹³⁵⁻¹³⁸ In terms of device performance, dye sensitized solar cells reached a plateau of 11% by the mid-1990s, with a portion of the losses coming from back-transfer to the electrolyte from the TiO₂ layer, essentially due to poor transport.¹³⁹⁻¹⁴¹ Groups then started to work with advanced nanoarchitectures with the aim of increasing electron diffusion lengths and improving cell efficiencies.¹⁴²⁻¹⁵⁰

2.2.4.3 One- Dimensional (1-D) transport architectures

By replacing nano-particulate films with 1-D architectures, charges are allowed to move only in one dimension instead of randomly in three dimensions. Many research have proven and reported

that the directed movement (1D) markedly improves cell currents and reduces losses by increasing the residence lifetime of charge carriers.¹⁵¹

One key to the 1-D architecture's improvement is to increase the diffusion length,¹⁵² which is validated as the form of a combination of larger crystal sizes, better contact between particles, and fewer trap sites, residence lifetimes of electrons were found by Frank et al. to be more than an order of magnitude longer than a similar nanoparticle film.¹⁵³ Figure 8 demonstrates the lower trap population in 1-D films. Other research groups has also indicated a 20% improvement in photocurrent by using TiO₂ nanotube in place of nanoparticles film.¹⁵⁴ Although 1-D architectures also change how the film absorbs light,¹⁵⁵⁻¹⁵⁸ the primary mechanism for improvement is the increased residence lifetime.

One-dimensional architectures like TiO₂ nanorods are typically synthesized on a substrate to keep uniform, parallel orientation of the 1-D axis normal to the substrate. Uniform orientation provides directionality in a system and allows for the possibility of each 1-D nanowire to have contact with the substrate, minimizing grain boundary crossings for charge carriers.¹⁵⁹⁻¹⁶⁰ Although both arguments for uniformity have the benefit of improving cell performance, several studies have shown that randomly oriented 1-D networks still provide exceptional enhancement with uniform networks only demonstrating a slight improvement over random networks. The primary mechanism for enhancement the solar cell efficiency is to improve diffusion length (stemming from the lifetime), which allows charge carriers to move through the metal oxide films more efficiently.¹⁶¹⁻¹⁶²

2.3 COLLOIDAL QUANTUM DOTS

2.3.1 Introduction

Colloidal quantum dots (CQDs) are nanometer-sized particles of the semiconductor, which are small enough to exhibit quantum mechanical properties. CQDs' physical dimensions and shape are all confined, which determines their optical and electrical properties.¹⁶³ The size-effect on the tunability differentiates them from other, non-quantum-confined nanocrystals, and the electronic properties of these materials are intermediate between bulk semiconductors and discrete molecules. By tuning the quantum dots size, great improvement in the properties and performance of solution processed solar cells, photodetectors,¹⁶⁴⁻¹⁶⁶ and light-emitting devices (LEDs) will be achieved.¹⁶⁷⁻¹⁶⁸ Nowadays a great attraction for colloidal quantum dots has been attracted for the photovoltaics solar cell researchers. Combination of wide-band-gap metal oxide semiconductors and CQDs also forms a class of CQD-based solar cells, in which metal oxides work as an electron carrier transportation and CQDs work as light absorbers and hole conductors. Specifically, PbS QDs have been widely used as photovoltaic materials.

2.3.2 Basics of Colloidal Synthesis: Nucleation and Growth

Normally the quantum dots fabricated via simple experimental equipment and low-cost allows researchers to obtain high quality materials.¹⁶⁹ At the meanwhile, their properties could be tuned

simply via change the size. Basically, colloidal quantum dots are fabricated by reacting corresponding inorganic salts or organometallic compounds molecular precursors. Additionally, there are mainly four procedures for fabricating the colloidal quantum dots: nucleation from initially homogeneous solution, growth of the preformed nuclei, isolation of particles reaching the desired size from the reaction mixture, post treatments, etc. Normally, the separation of the nucleation from the growth of the nuclei could be achieved through two ways¹⁷⁰⁻¹⁷¹, one is the so-called hot-injection technique, which means that precursors are rapidly poured into a hot solvent with subsequent temperature drop¹⁷²⁻¹⁷³ Another ways is to heat the reaction mixture steadily.¹⁷⁴

Nucleation and growth of nanocrystals (NCs) occur in the solution phase in the presence of organic surfactant molecules that dynamically adhere to the surface of growing crystals,¹⁷⁵ such as long-chain carboxylic and phosphonic acids , alkanethiols, alkyl phosphines, alkylphosphine oxides and alkylamines. Therefore, the surfactant molecules have the key effect on tuning the kinetics of nanocrystals nucleation and growth,¹⁷⁶ which are required to be balanced kinetically. Compared with the growth rate, if the nanoparticle nucleation rate is too slow, the reaction generates bulk crystals. In the opposite way, if the rate of the nanocrystals nucleation is too fast, the reaction generates molecular clusters. Thus, a good combination of molecular precursors, surfactants, solvent, and the reaction conditions for the nucleation and growth is very critical, and it is very practical to study the fundamental fabrication methods for producing the quantum dots with the uniform size shape, composition, and surface morphology.

Lots of methods can be used to tune the size of nanocrystals during fabrication. Normally, It hardly dominates the reaction at the desired stage of particle growth, because that the nanocrystals nucleate and grow in a very short time. There are two main approaches. One is to adjust the nanoparticle size via making the small nanoparticles first. The purpose of the small nanoparticles is for further growth by adding appropriate amounts of molecular precursors as a function of seeds. Another common way is via controlling the relative nucleation and growth rates of nanocrystals. It is assumed that the total amount of molecular precursors is constant during the reaction. The faster nucleation rate is, the higher concentration of nuclei is. Further it results in smaller size nanocrystals. In another aspect, slow nucleation provides low concentration of seeds which using the same amount of precursors, thus yields larger particles. Moreover, by changing the reaction temperature, the balance between nucleation and growth rates can be changed, due to the reason that the activation energy for the homogeneous nucleation is usually much higher than that for particle growth.¹⁷⁷ After many research investigated, the increase of reaction temperature could obtain smaller NCs for different materials. Like the reaction temperature, tuning nature and concentration of capping molecules, molar ratios of precursors are also other approaches to change the particle size.

Semiconductor nanocrystals now makes great progress in fabrication. Figure 9 shows examples of colloidal semiconductor. Typical syntheses of II-VI (CdSe, CdTe, CdS),¹⁷⁸⁻¹⁸² III-V (InP, InAs),¹⁸³⁻¹⁸⁶ and IV-VI (PbS,¹⁸⁷⁻¹⁹¹ PbSe, PbTe¹⁹²) semiconductor NCs are normally synthesized at high temperatures, and in the presence of long-chain alkylphosphines (e.g.,

trioctylphosphine, TOP), alkylphosphine oxides (e.g., trioctylphosphine oxide, TOPO), alkylamines (e.g., hexadecylamine, HDA), and alkylphosphonic acids as the stabilizing agents.

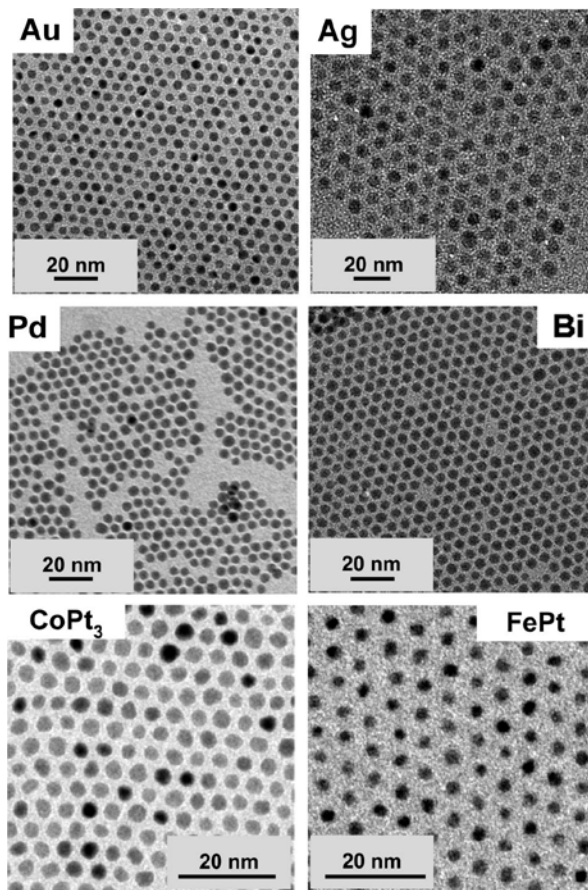


Figure 9. Examples of synthesized metal and metal alloy nanoparticles³⁸

Basically, the size of semiconductor NCs can be changed by many factors, such as tuning the concentrations of surfactants, reaction temperature, and duration of the particle growth. Moreover, in a typical colloidal solution, semiconductor NCs often grow through the mechanism called Ostwald ripening, which means the largest particles in solution are at the cost of dissolving smaller ones. Thus, average particle size increases with time, oppositely, the particle

concentration decreases. Lots of researches focused on the kinetics of nanoparticle growth and dissolution to simulate this self-consistent growth process and investigate the factors terminating particle size distribution during the fabrication of semiconductor NCs. Peng et al describes theory of the “focusing” and “defocusing” on size distribution in the nanocrystals growth.¹⁹³⁻¹⁹⁴ Also, “Nano-Ostwald ripening” was established to describe the basic model for nanocrystals ensemble.¹⁹⁵

The quantum confinement effect for nanocrystals semiconductors is more related to the nanoparticles electronic structure and its size. Comparison with the bulk semiconductor materials, the nanocrystals semiconductors exhibit discrete electron and hole states that can be easily tuned via changing the nanoparticles size. Also, by applying with the appropriate surface chemistry, the mid-gap states can be removed, which have the relationship with surface dangling bonds. From the literature studying, high (>80%) luminescence quantum efficiencies of nanocrystals semiconductors were observed by decreasing possible carrier trapping and nonradiative recombination.¹⁹⁶⁻¹⁹⁹

2.3.3 Electronic Structure and Shell Filling of Semiconductor Nanocrystals

It is very important to investigate the carrier transport knowledge in depth for improving the efficiency of the nanocrystals-based solar cells. As introduced above, the electronic structure of semiconductor NCs is formed by strong quantum confinement. Unlike bulk semiconductors, the

electronic structure of nanocrystals are discrete electron and hole states, which is described as the quantum confined orbitals (Figure 10). The size and shape of the nanocrystals dominate its corresponding energies in a direct way. The series of electron and hole states with S, P, D, and F symmetries for spherical nanocrystals, which are the same as the hydrogen atom energy levels (Figure 10). The electron and hole states will be marked as the “e” and “h” indexes, respectively. The degeneracy of the quantum confined states is determined by symmetry of NC atomic lattice . Thus, NCs with wurtzite and zinc blend lattices typical for most II-VI and III-V semiconductors have 2-, 6-, and 10-fold degenerated $1S_e$, $1P_e$, and $1D_e$ states, respectively. For example, PbS, PbSe, and PbTe NCs with rock salt lattices have 4 times higher degeneracy and can adjust up to eight electrons on their $1S_e$ and $1S_h$ states.²⁰⁰ Typically, in a nanocrystals with neutral charge, the highest occupied ($1S_h$) and lowest unoccupied ($1S_e$) states are separated by the forbidden energy gap which is much larger than the thermal energy $k_B T$ (25 meV at 300 K), and thus electrons cannot be thermally excited into $1S_e$ state. Normally semiconductor NCs do not contain conduction electrons and holes in the neutral ground state, and additional carriers should be produced in a way by photo-excitation to make the nanocrystals semiconductors conductive. In addition, the conductivity of nanocrystals materials depends on the number of conduction electrons or holes per nanocrystals and their mobility is determined by the tunneling rate. In strongly confined NCs, the gaps between S, P, and D states is much greater than the thermal energy, and additional carriers in an order occupy the quantum confined states following the Pauli principle.¹⁹⁶⁻¹⁹⁷ Banin *et al.* found sequential filling of the quantum confined states in NC quantum dots using scanning tunneling spectroscopy .²⁰¹ Each Addition of electron to the NC

consumes the Coulombic charging energy (E_c) and the energy of electrostatic repulsion between the incoming electron and the additional electron exist in the NC (E_{c-e}). These factors lift degeneracy of the S, P, and D states (Figure 10).

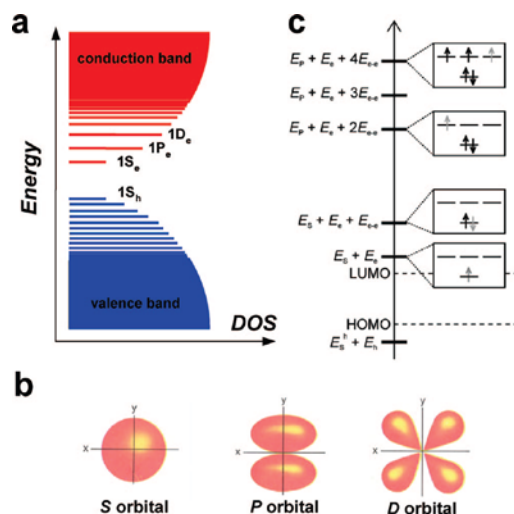


Figure 10. (a) Size-dependent electronic structure of individual semiconductor nanocrystals (b) Electronic states in the valence and conduction bands corresponding to the atomic-like S, P and D orbitals (c) The electrochemical potentials for sequential additions of electrons to typical semiconductor nanocrystals³⁸

2.3.4 Multiple Exciton Generation in Semiconductor Quantum Dots

The efficient formation of more than one photo-induced electron– hole (e_-h_+) pair by the absorption of a single photon from solar energy is potentially critical for photovoltaic devices, which can improve the efficiency of the direct conversion of solar irradiance to electricity. During this process, the excess kinetic energy of electrons and holes produced in photovoltaic

solar cell by absorbing the photons with energies above the threshold energy for absorption, which indicates the bandgap in semiconductors and the highest occupied molecular orbital and lowest occupied molecular orbitals (HOMO–LUMO) energy difference in molecular systems. The excessive thermal energy raises additional electron-hole pairs when the photon energy is at least twice the bandgap or HOMO–LUMO energy. In a result, the extra electrons and holes can be separated, transported, and collected to lead to higher photocurrents in the photovoltaic solar cell. Therefore, the conversion efficiency increases. In most cases, excess kinetic energy of photoconversion cells is converted to heat and becomes unavailable for conversion to electrical or chemical free energy as a form of thermal loss, thus limiting the maximum conversion efficiency²⁰²⁻²⁰⁵.

Similarly, the creation of more than one e^- - h^+ pair per absorbed photon has been also found in the photocurrent of bulk p–n junctions in Si, Ge, PbS, PbSe, PbTe, and InSb, and in these systems is a process called impact ionization. However, compared with the quantum dots, impact ionization in bulk semiconductors is relatively not an efficient process and the threshold for the photon energy to meet the requirement is as many multiples as the threshold value of the absorption energy.

However, for the colloidal quantum dots, the generation of multiple e^- - h^+ pairs from a single photon is very efficient and the threshold photon energy for the process to generate two electron–hole pairs per photon can be the values as low as twice the threshold energy for absorption, which is the absolute minimum to meet energy conservation requirement. More importantly, multiple exciton effect satisfies the threshold to occur in the visible or near-IR

spectral region. In semiconductor QDs, the $e^- - h^+$ pairs are related because of the spatial confinement and thus exist as excitons. As a result, formation of multiple excitons in quantum dots is defined as multiple exciton generation (MEG). As mentioned above, for quantum dots, the rate of electron relaxation through electron–phonon interactions can be greatly decreased because of the discrete property of the $e^- - h^+$ spectra, and the rate of Auger processes. Specifically, the inverse Auger process is significantly increased for the reason of carrier confinement and the increased $e^- - h^+$ Coulomb interaction. As mentioned in the literature, the well-defined location of the electrons and holes in the nanocrystals makes the momentum uncertain, which comes from the Heisenberg Uncertainty Principle. It indicated that crystal momentum need not be conserved due to that momentum is not a beneficial quantum number for three-dimensionally confined carriers. The concept of enhanced MEG in quantum dots is described in Figure 11. Nowadays, very efficient multiple $e^- - h^+$ pair (multi exciton) creation by one photon has now been reported mainly among six semiconductor QD materials: PbSe, PbS, PbTe, CdSe, InAs.

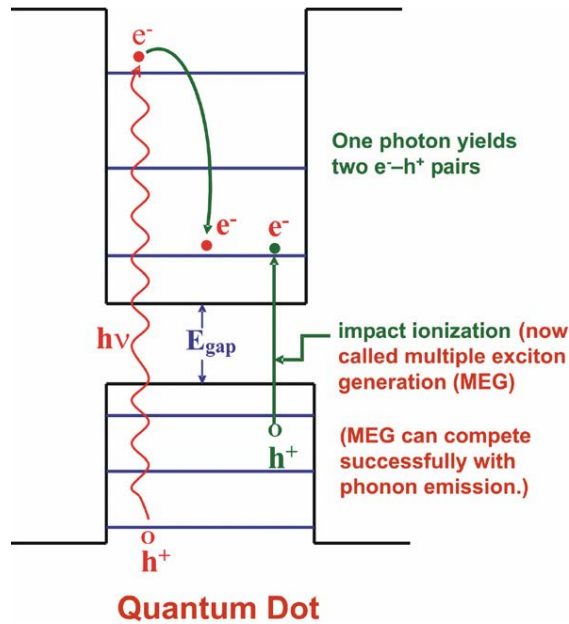


Figure 11. Multiple electron-hole pair (exciton) generation (MEG) in quantum dots²⁰⁶

2.4 DEVICE APPLICATION AND COMPARISON

This chapter simply describes the device architecture and concepts that allow colloidal quantum dot (CQD) solar cells to achieve the balance among the V_{oc} , J_{sc} , and FF.

Colloidal quantum dot photovoltaics application²⁰⁷⁻²⁰⁸ offers a widely tunable bandgap property, which enables both single-junction cells and multijunction architectures. Size-effect tuning also provides the possibility for using of low cost and narrow bandgap semiconductors previously unsuited for photovoltaic energy conversion.²⁰⁹

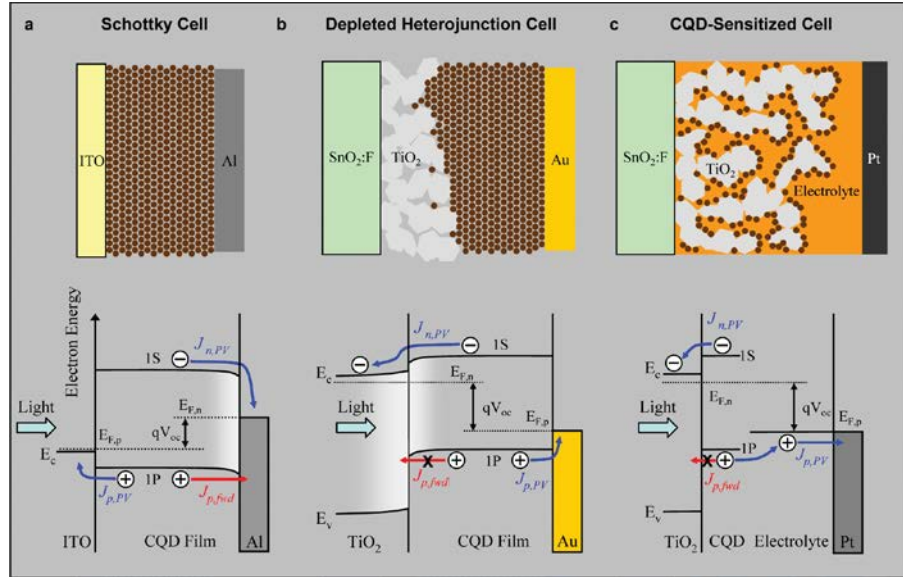


Figure 12. Comparison of three CQD photovoltaic architectures²¹⁰

Figure 12 compares the three different colloidal quantum dots photovoltaic solar cell structures, which are the Schottky barrier device architecture, the DH-CQD device and the CQD-SSC respectively. In the figure spatial band diagrams are applied to introduce the behavior of CQD films combined with metal contacts and heterojunctions with other semiconductors. Both the Schottky and the DH architectures exhibit a depletion layer that increases from charge transfer from the electron-accepting contact to the p-type CQD film. Due to a very high free electron density for metals²¹¹, there is almost no depletion region on the metal side of the Schottky junction. In contrast, in the DH-CQD device, the TiO₂ electrode is partially depleted via its lower n-type carrier density.

The Schottky device is disadvantaged by many aspects. Firstly, as light absorption begins at the Ohmically contacted side instead of the junction, many minority carriers (here electrons)

must travel the thickness of the entire film before reaching their destination electrode and are therefore more susceptible to recombination. The DH design, with the transparent electron accepting TiO₂ contact, benefits from minority carrier separation due to the placement of the junction on the light injection side. Second, in the Schottky device, the open-circuit voltage is often limited by Fermi-level pinning due to defect states at the metal-semiconductor interface.²¹¹ In contrast, the TiO₂-CQD interface may be passivated during the solution-phase deposition of the quantum dots. Third, the barrier to hole injection into the electron-extracting electrode of the Schottky device becomes much less effective when the device is operating in the photovoltaic quadrant. Both the DH and the CQD-SSC approaches mitigate this effect by introducing a large discontinuity in the valence band and by minimizing the electron density in the electron acceptor near the junction. The CQD-SSC architecture can show good V_{oc} and FF since the electrolyte, whether solid or liquid, is usually a good hole transporter, and back-recombination of electrons and holes across the TiO₂-electrolyte interface can be blocked. However, a CQD monolayer adsorbed on the TiO₂ surface has a lower absorption coefficient than similarly created dye layers, and as such high J_{sc} values cannot be reached without the cost of the FF. In an opposite way, the DH architecture can employ many monolayers of the light absorber due to the charge-transporting functionality of the CQD film.

2.5 FINITE DIFFERENCE TIME-DOMIAN (FDTD) TECHNIQUE

2.5.1 Introduction

The FDTD algorithm is useful for design and investigation in a wide variety of applications involving the propagation of electromagnetic radiation through complicated media. It is especially useful for describing radiation incident upon or propagating through structures with strong scattering or diffractive properties. The available alternative computational methods - often relying on approximate models - frequently provide inaccurate results.

The Finite Difference Time Domain (FDTD) method has become the state-of-the-art method for solving Maxwell's equations in complex geometries.²¹²⁻²¹³ It is a fully vectorial method that naturally gives both time domain, and frequency domain information to the user, offering unique insight into all types of problems and applications in electromagnetics and photonics.

The technique is discrete in both space and time. The electromagnetic fields and structural materials of interest are described on a discrete mesh made up of so-called Yee cells. Maxwell's equations are solved discretely in time, where the time step used is related to the mesh size through the speed of light. This technique is an exact representation of Maxwell's equations in the limit that the mesh cell size goes to zero.

Structures to be simulated can have a wide variety of electromagnetic material properties. Light sources may be added to the simulation. The FDTD method is used to calculate how the

EM fields propagate from the source through the structure. Subsequent iteration results in the electromagnetic field propagation in time. Typically, the simulation is run until there are essentially no electromagnetic fields left in the simulation region. Time domain information can be recorded at any spatial point (or group of points). Frequency domain information at any spatial point (or group of points) may be obtained through the Fourier transform of the time domain information at that point. Thus, the frequency dependence of power flow and modal profiles may be obtained over a wide range of frequencies from a single simulation.

Here will introduce the basic mathematical and physics formalism behind the FDTD algorithm. FDTD solves Maxwell's curl equations in non-magnetic materials:

$$\frac{\partial \vec{D}}{\partial t} = \nabla \times \vec{H} \quad (12)$$

$$\vec{D}(\omega) = \varepsilon_0 \varepsilon_r(\omega) \vec{E}(\omega) \quad (13)$$

$$\frac{\partial \vec{H}}{\partial t} = -\frac{1}{\mu_0} \nabla \times \vec{E} \quad (14)$$

where H, E, and D are the magnetic, electric, and displacement fields, respectively, while $\varepsilon_r(\omega)$ is the complex relative dielectric constant ($\varepsilon_r(\omega) = n^2$, where n is the refractive index).

In three dimensions, Maxwell equations have six electromagnetic field components: E_x , E_y , E_z and H_x , H_y , and H_z . On the assumption that the structure is infinite in the z dimension and that the fields are independent of z, specifically that

$$\varepsilon_r(\omega, x, y, z) = \varepsilon_r(\omega, x, y) \quad (15)$$

$$\frac{\partial \vec{E}}{\partial z} = \frac{\partial \vec{H}}{\partial z} = 0 \quad (16)$$

Then Maxwell's equations split into two independent sets of equations composed of three vector quantities each which can be solved in the x-y plane only. One is termed the TE (transverse electric), and the other is TM (transverse magnetic) equations. We can solve both sets of equations with the following components:

$$TE: E_x, E_y, E_z \quad (17)$$

$$TM: H_x, H_y, H_z \quad (18)$$

For example, in the TM case, Maxwell's equations reduce to:

$$\frac{\partial D_z}{\partial t} = \frac{\partial H_y}{\partial x} - \frac{\partial H_x}{\partial y} \quad (19)$$

$$D_z(\omega) = \epsilon_0 \epsilon_r(\omega) E_z(\omega) \quad (20)$$

$$\frac{\partial H_y}{\partial t} = -\mu_0 \frac{\partial E_z}{\partial y} \quad (21)$$

$$\frac{\partial H_x}{\partial t} = \mu_0 \frac{\partial E_z}{\partial x} \quad (22)$$

The FDTD method solves these equations on a discrete spatial and temporal grid. Each field component is solved at a slightly different location within the grid cell (Yee cell), as shown in Figure 13 below. By default, data collected from the FDTD solver is automatically interpolated to the origin of each grid point, so the end user does not have to deal with this issue in their analysis.

Dispersive materials with tabulated refractive index (n,k) data as a function of wavelength can be incorporated by using the multi-coefficient material models that automatically generates a material model based on the tabulated data. Alternatively, specific models such as Plasma (Drude), Debye or Lorentz can be used. The FDTD solver supports a range of boundary conditions, such as PML, periodic, and Bloch. Also, the FDTD solver supports a number of different types of sources such as point dipoles, beams, plane waves, a total-field scattered-field (TFSF) source, a guided-mode source for integrated optical components, and an imported source to interface with external photonic design softwares.

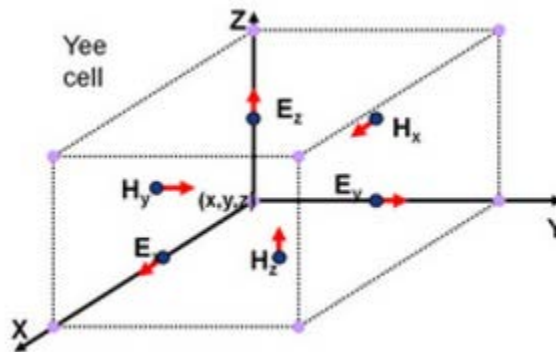


Figure 13. Yee Cell ²¹²

2.5.2 FDTD modeling of solar energy absorption in PbS sensitized TiO₂ nanorods

Although many studies focused on the nanostructured materials, research in TiO₂ nanowire (NW) solar cells is still relatively new compared to thin film bulk solar cells. Besides cell efficiency, there are differences between the materials and processing of planar and nanowire solar cells. In

planar TiO_2 devices, as shown in Figure 14, high absorbed material is required in order to maximize absorption of the incident solar radiation and achieve sufficiently long minority carrier diffusion lengths. Planar cells that use (less expensive) materials with a higher level of impurities and crystalline defects typically leads to a reduction in the minority carrier diffusion length and thus reduced cell efficiency. The p-n junctions in the nanowire arrays are radial, as shown in Figure 14, with very short diffusion distances. This configuration allows the use of less expensive materials with higher level of impurities and crystalline defects. TiO_2 NW arrays occupy a fraction of the array volume with wafer based devices and have shown to exceed the ray-optics light-trapping absorption limit of an equivalent volume of textured planar material. TiO_2 nanowire cells show a broadband, near unity internal quantum efficiency for carrier generation because of relatively short diffusion lengths for the minority carriers. Maximizing efficiency requires that the wire array provide high absorption and be sized for efficient carrier collection.

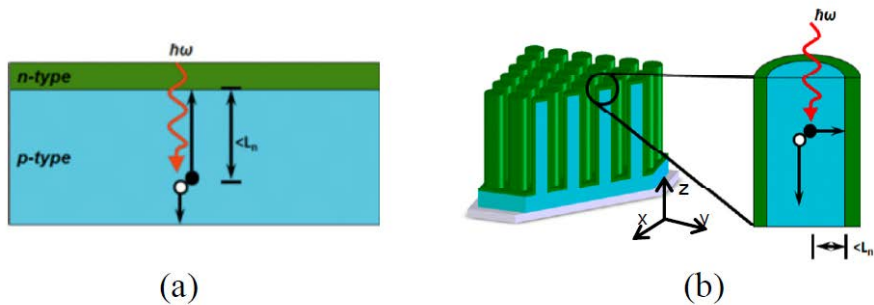


Figure 14.light and carrier interactions between p-n junction (a) planar junction (b) radial junction

Prior studies of branched nanowires primarily focused on experimental investigations of nanowire synthesis and characterization of the structural and optical properties of the resulting nanostructured surfaces. This work has been the topic of several recent review researches.

A finite-difference time-domain (FDTD) 3-dimensional electromagnetic field simulation package, was used to model the nanowire arrays. FDTD is a good choice to model a wide bandwidth, since it uses a time-domain pulse made up of multiple frequencies. Additionally, It is possible to obtain good results for optical reflection using only a single frequency independent value for the real part of the material dielectric constant. However, modeling absorption requires the use of the imaginary part of the dielectric constant as well.

Lumerical solutions provides the computational methods for accurately solving Maxwell's equations for arbitrary 3D geometries such as the Finite Difference Time Domain method combined with computer aided design and analysis provide a powerful platform research and development in nanophotonics.

3.0 METHODOLOGY

3.1 TiO₂ NANOWIRE FABRICATION AND CHARACTERIZATION

In a typical synthesis, 53 mL of deionized water was mixed with 67 mL of concentrated hydrochloric acid (36.5%-38% by weight) to reach a total volume of 60 mL in a Teflon-lined stainless steel autoclave (125 mL volume, Parr Instrument Co.). The mixture was stirred at ambient conditions for 5 min before the addition of 1 mL of titanium butoxide (97% Aldrich). After stirring for another 5 min, two pieces of fluorine-doped tin oxide (FTO) substrates, ultrasonically cleaned for 60 min in a mixed solution of deionized water, acetone, and 2-propanol with volume ratios of 1:1:1, were placed at an angle against the wall of the Teflon-liner with the conducting side facing down. The hydrothermal synthesis was conducted at 180-220 °C for 18-25min in a microwave oven. After synthesis, the FTO substrate was taken out, rinsed extensively with deionized water and allowed to dry in ambient air.

Scanning electron microscopy (SEM) images were obtained with a Philips XL-30 field emission gun scanning electron microscope. Samples were coated with Au/Pd prior to observation. X-Ray diffraction (XRD) measurements were made on a Philips PW1710 diffractometer with monochromated Cu radiation.

3.2 FDTD SIMULATION AND MODELING

This research describes the application of FDTD analysis in Quantum Dots based solar cells fabricated with titania nanotube arrays, grown from titanium thin films, as negative electrodes. The thin film approach provides the advantage of using front side illumination with light passing through the TCO glass and the PbS-coated nanotube array where the energy loss in the visible wavelength range is less compared to the backside illumination in which case, the light passes through the platinized TCO and the electrolyte before striking the nanotube arrays. Figure 15 shows a schematic of the front illuminated DSC structure with a titania nanotube array cathode.

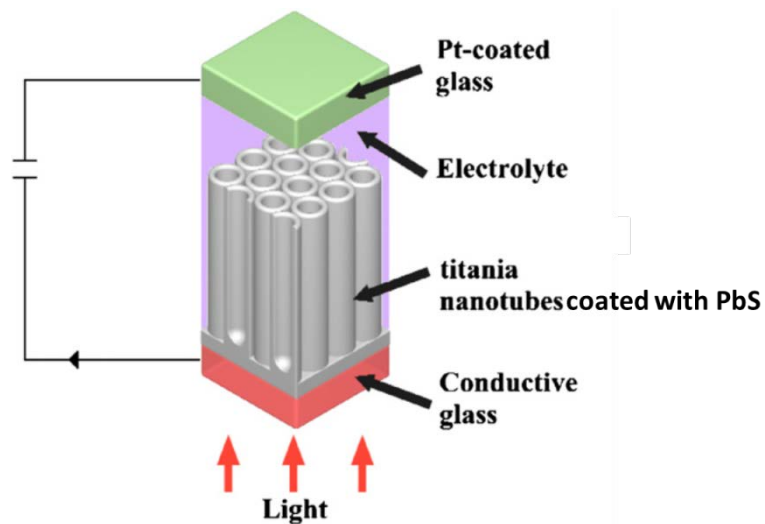


Figure 15. A schematic of the titania nanotube quantum dots-sensitized solar cell

The numerical model used in this work is shown in Figure 16. Nine nanowire array dimensions are defined by the length L , diameter of the wire d_i , wall thickness (PbS layer) w , and barrier titania layer thickness d_b . The separation distance between two adjacent tubes was kept

constant at 10 nm, and wall thickness was set at 12 nm. The transparent conductive substrate supporting the nanotube array was omitted in the model (100% light transmission), while the positive electrode was represented by a perfect electric conductor (PEC) with 100% light reflection. To avoid complexity, the effect of the electrolyte is not considered in this research; light losses between the top of the nanotube array and PEC are not taken into account. In this model, the nanotubes were covered with a PbS-covered layer 12 nm thick. The FDTD space was terminated with an absorbing boundary condition made of uniaxial perfect matching layer to absorb any stray fields for z-direction, and the periodic Boundary conditions for the x and y planes. The grid size of the FDTD model was set to $2 \times 2 \text{ nm}^2$.

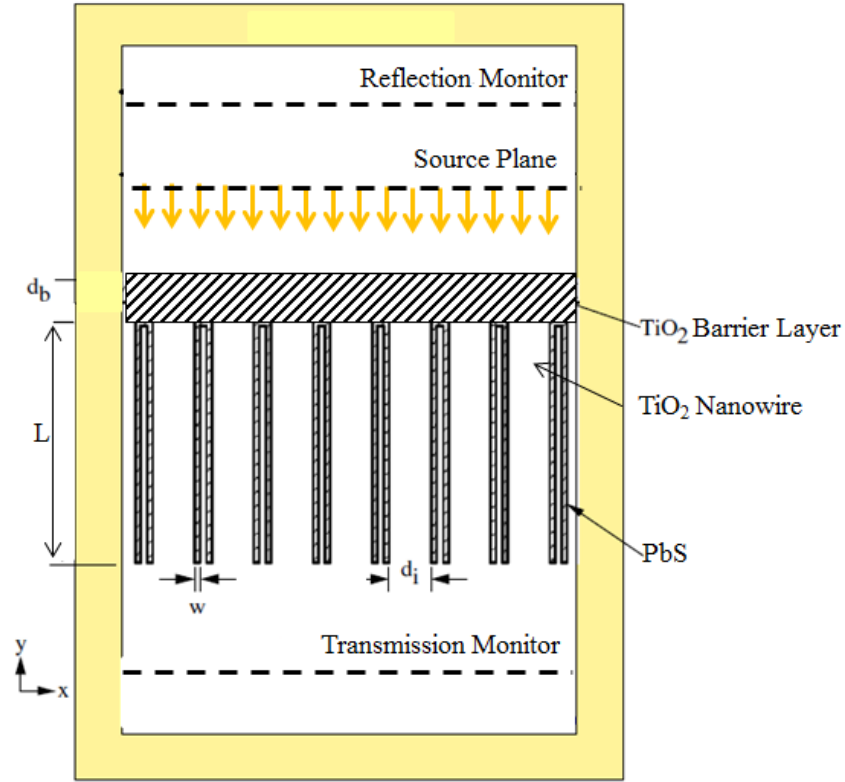


Figure 16. A schematic for two-dimensional FDTD model

The excitation wave, generated at the source plane located above the barrier layer of the nanotube array, is a transverse electromagnetic (TEM) wave propagating along the y -axis of a rectangular coordinate TEM_y system. The excitation source is chosen as a modulated Gaussian electric field, which is a sinusoidal wave windowed by a Gaussian pulse. The modulated Gaussian source can be expressed in the time domain as

$$E_i(t) = E_0 e^{-(t-t_0)^2/t_w^2} \sin(2\pi f_m t) \hat{x} \quad (23)$$

where E_0 is the field strength, t_0 the time delay before the beginning of the Gaussian pulse, t_w the Gaussian pulse width, f_m the frequency of the sinusoidal component, and \hat{x} indicates the

direction of the excitation wave. We ignore the effect of the reflected field E_r from the barrier layer since it forms only a small part of the excitation field due to the low refractive index of titanium dioxide, 1.5–2.5 for a dense film, and it does not interact with the PbS-coated nanowires. The transmitted wave propagates through the barrier layer and PbS-coated nanowires before being reflected from the PEC. This reflected wave travels back through nanotube array and barrier layer and reaches the reflection monitor plane carrying information about light–material interactions, Also a transmission monitor plane is also placed under the PbS-coated nanowires.

By performing a fast Fourier transformation calculation on electric and magnetic field during the simulation, the transmission function returns the amount of power transmitted through power monitors and profile monitors, normalized to the source power. A value of 0.5 means that half of the optical power injected by the source passed through the monitor. Negative values mean the power is flowing in the negative direction.

The transmission is calculated with the following formula.

$$T(f) = \frac{\frac{1}{2} \int \text{real}(\vec{P}(f)^{Monitor} \cdot d\vec{s})}{sourcepower}} \quad (24)$$

Where $T(f)$ is the normalized transmission as a function of frequency, $P(f)$ is the Poynting vector and dS is the surface normal.

In order to investigate the influence of the NW dimensions on the light scattering, the spectral dependence of the total transmission of the PbS coated titania arrays was analyzed. The

optical transmittance T and reflectance R were measured from 300 to 700 nm via the FDTD simulation and which are allowed to calculate the absorption A . And A equals to $1-R-T$.

The optical constant of titania and PbS with the wavelength as shown in Figure 18, Figure 19 and Figure 20 below.

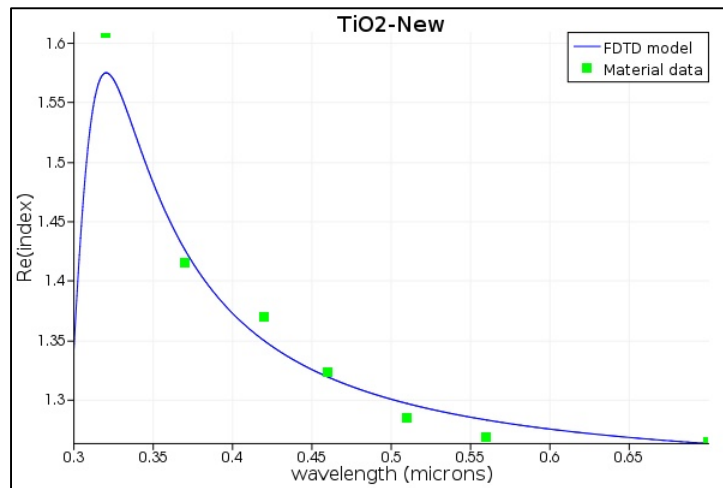


Figure 17. Optical constant spectra of titania-n

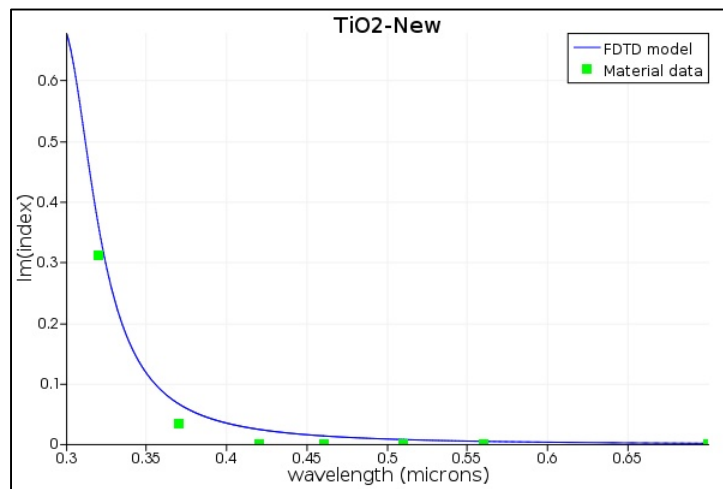


Figure 18. Optical constant spectra of titania-k

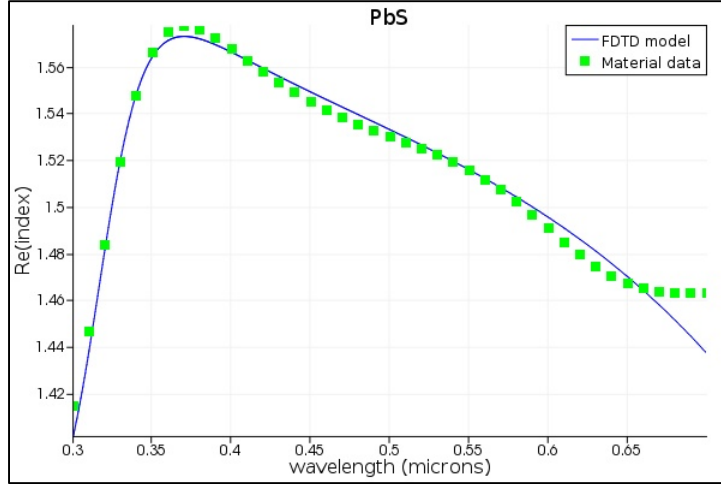


Figure 19 .Optical constant spectra of PbS-n

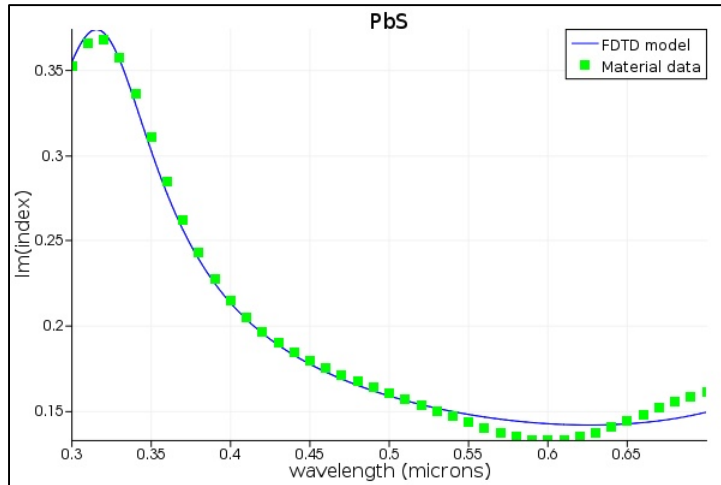


Figure 20. Optical constant spectra of PbS-k

In summary, the light scattering in TiO₂ NW arrays and the influence on their solar light sensitization have been studied. The intensity and wavelength of the scattered light depend mainly on the NW length and diameter, respectively. The optical engineering has been shown to be a very attractive strategy for the sensitization of TiO₂ NW arrays to solar light. An effective

absorption, in the 300–700 nm of the AM1.5 solar spectrum range will be used for the FDTD simulation.

4.0 RESULTS AND ANALYSIS

4.1 RESULTS FOR COMPUTATIONAL MODEL

4.1.1 Simulation Modeling

Figure 21 is the simulation workspace window for TiO₂ nanowire simulation via the software FDTD solutions created via Lumerical Solution Inc. The nanowire length is 1 μ m, and radius is 22nm, the no PbS, and the space between each nanowire is 10nm.

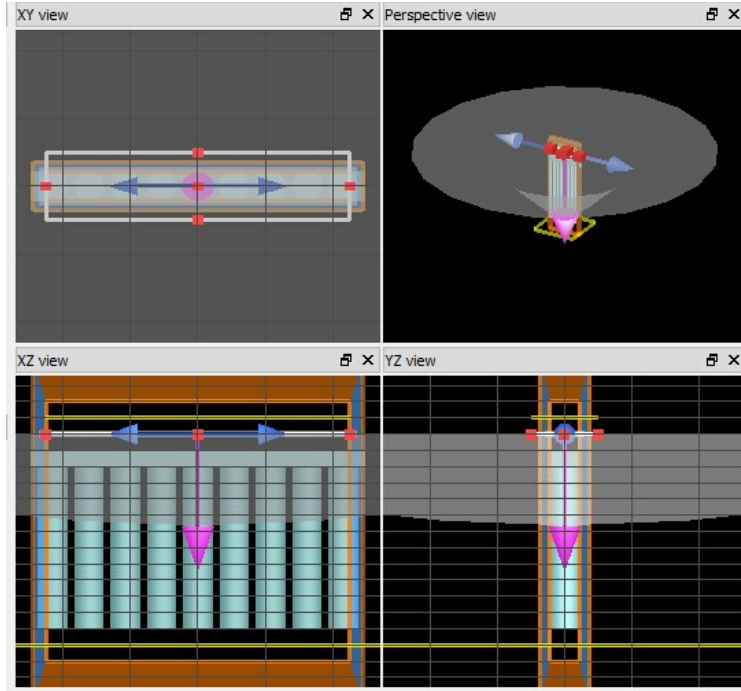


Figure 21. Simulation window for the titania arrays

Figure 22 is the simulation workspace window for the PbS coated nanowire simulation via the software FDTD solutions created via Lumerical Solution Inc. The nanowire length is 1 μ m, and radius is 22nm, the PbS coating wall thickness is 12nm, and the space between each nanowire is 10nm.

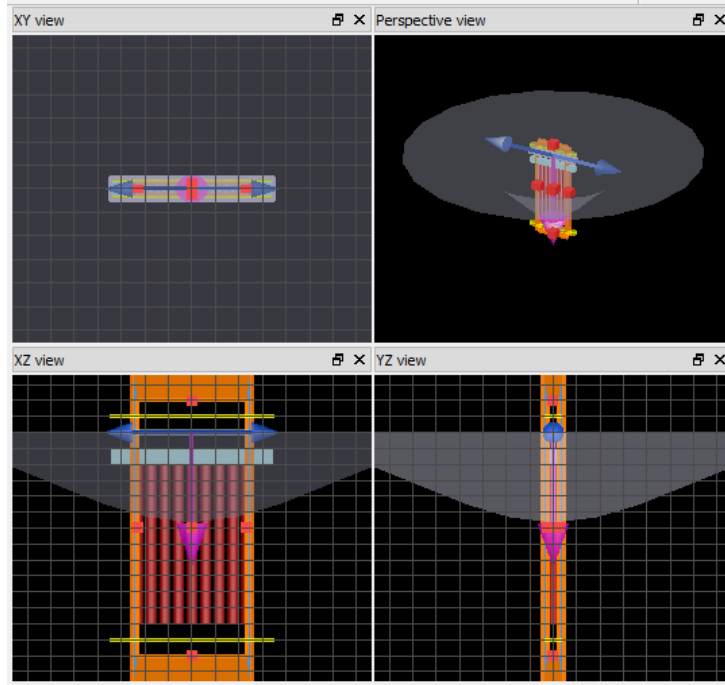


Figure 22. Simulation window for the titania based quantum dots solar cell

4.1.2 Data Analysis

The light transmittance and absorbance through the titania nanowire model are calculated as functions of nanowire length L , radius d_i , barrier layer thickness d_b , , while keeping the average PbS wall thickness at 12nm and nanowire and nanowire separation 10 nm.

Figure 23 indicates that both FDTD simulated and experimentally measured results are similar with minor differences in the transmission for pure TiO_2 nanorods with thickness 200nm and radius 50nm. These differences might be due to the errors in the determination of the refractive index 'n' and extinction coefficient 'k' of titania nanorods in the FDTD simulation and

real experiment part. Also, because FDTD simulation is a tool using the finite different calculation method, the difference in various geometrical features, including value of thickness, as well as surface toughness is unavoidable.

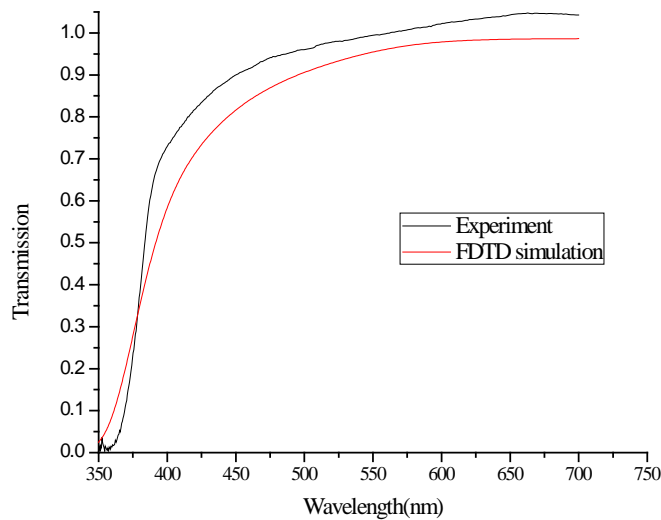


Figure 23. The comparison transmission data between experiment and FDTD simulation

Figure 24 and Figure 25 plot the transmittance and absorbance, respectively, which consist of 1000 and 200nm long titania nanotubes ($w= 12 \text{ nm}$, $d_b=100 \text{ nm}$, $d_i= 22 \text{ nm}$), with and without the PbS coating. As the band gap of the titania nanorods is approximately 3.2 eV, the absorption of light by the titania nanowires dominates at lower wavelengths and hence the effect of PbS quantum dots cannot be discerned. Therefore, only wavelengths above 300 nm were considered in the simulation. The influence of PbS coated on the titania nanorods array is evident in the case of higher length nanorods. The 1000 nm long nanotubes have a geometric surface

area five times that of 200nm nanotubes (with other dimensions same, such as pore size) and hence, it contains much higher amount of PbS quantum dots leading to greater light absorption.

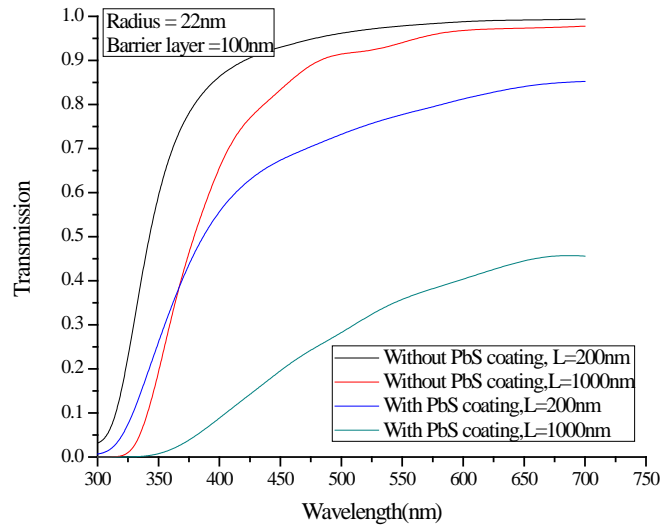


Figure 24. FDTD simulated transmission of titania-based solar cell of 1000 and 200nm in length with and without PbS coating

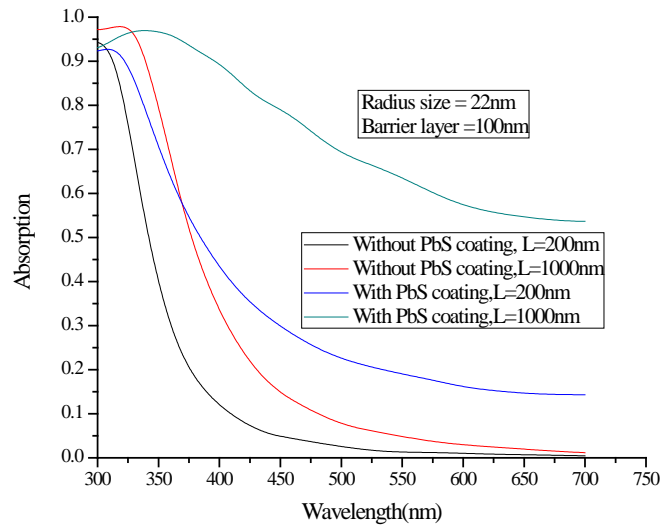


Figure 25. FDTD simulated absorption of titania-based solar cell of 1000 and 200nm in length with and without PbS coating

Figure 26 and Figure 27 is plotted to show the effect of length more clearly on the transmittance Figure 26 and absorbance Figure 27 of PbS-coated samples. As the absorption of visible light by the PbS peaks near 320 nm, see as the shift in absorbance/ transmittance is largest after the wavelength range 32-350 nm (Figure 26 and Figure 27). Thus higher absorption of the light by PbS quantum dots is a necessary, though not sufficient, condition for better solar cell performance. Although we have limited our efforts to a nanowire length of 1000nm due to technical limitations such as computer processing speed and memory requirement , Figure 26 clearly demonstrates that on extending the FDTD simulations to greater nanotube array lengths it should be possible to find an optimum length for the PbS-coated nanotubes for maximum light absorption. Figure 27 shows the percentage light absorption with nanotube array length.

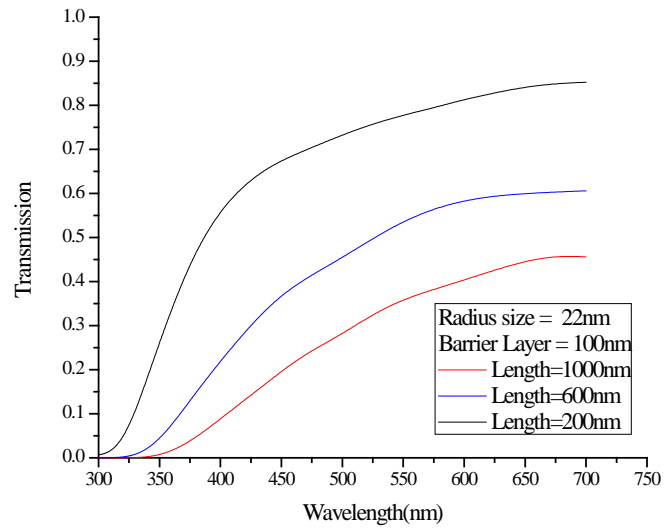


Figure 26.FDTD simulated transmission of titania- based quantum-dots solar cell as a function of nanowire length

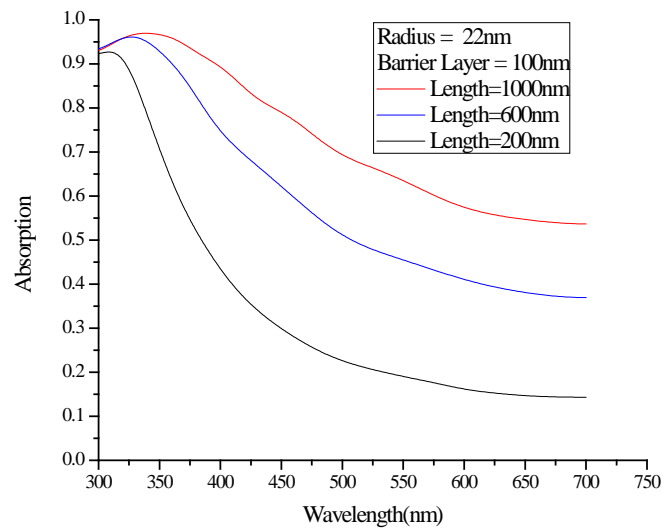


Figure 27 .FDTD simulated absorption of titania- based quantum-dots solar cell as a function of nanowire length

Figure 28 and Figure 29 show, respectively, the light transmission and absorption of the PbS-coated titania nanowires at varying radius, while the length of the wire, the wall thickness, and the barrier layer thickness are fixed. As shown in the figures, for a given nanowire length, wall thickness and barrier layer thickness, the light absorption increases with smaller nanowire radius indicating greater PbS coverage for the array with narrower wires.

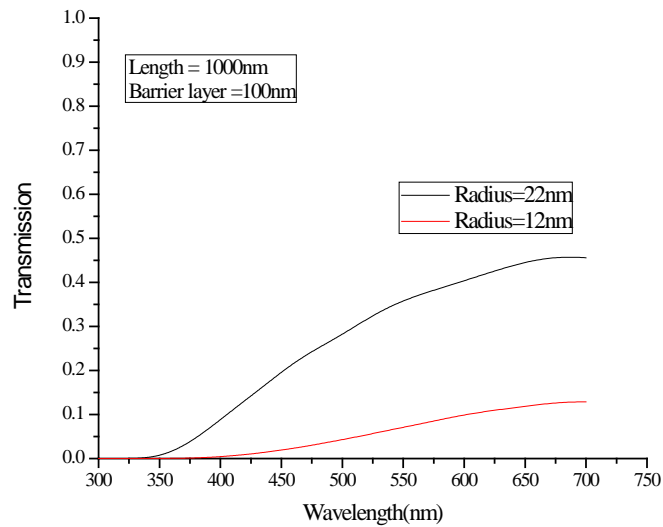


Figure 28. FDTD simulated transmission of titania- based quantum-dots solar cell as a function of radius

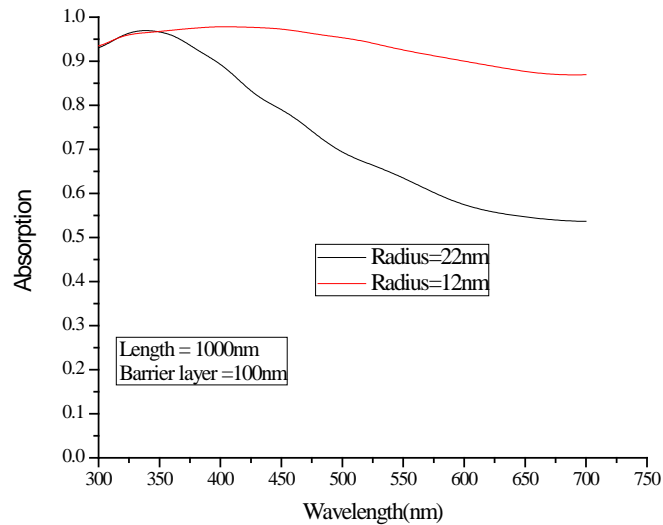


Figure 29. FDTD simulated absorption of titania- based quantum-dots solar cell as a function of radius

Additionally, Figure 30 and Figure 31 plot, respectively, the transmission and absorption of nanowire arrays with two different barrier layer thicknesses. As shown in the plot, varying the barrier layer thickness has negligible effect on the transmission and the absorption (as well as the initial reflection of the incident wave). This is consistent with the fact that increasing the barrier layer thickness does not increase the PbS coverage. However, a small increase in absorption (Figure 31) can be seen, which is believed is due to the absorption associated with the passage of light through the thick titania barrier layer.

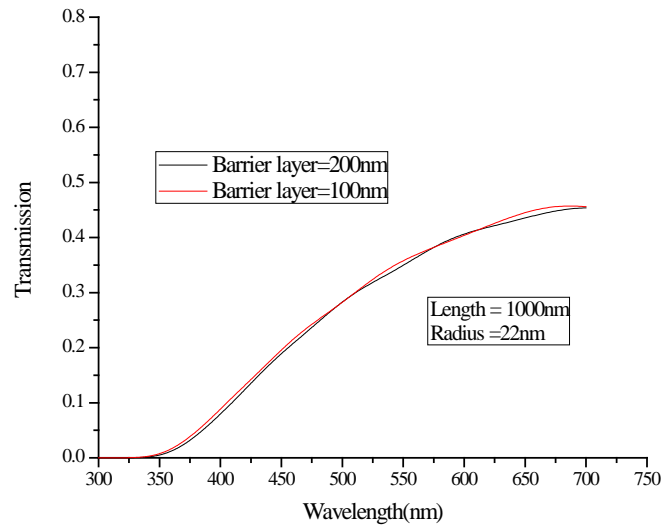


Figure 30. FDTD simulated transmission of titania- based quantum-dots solar cell as a function of barrier layer

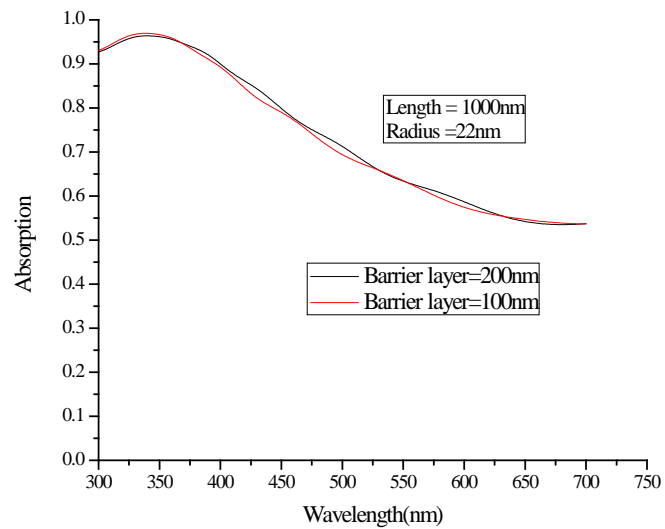


Figure 31. FDTD simulated absorption of titania- based quantum-dots solar cell as a function of pore size (radius)

4.2 EXPERIMENT

Figure 32 shows SEM micrographs of cross sections of the arrays constituted of the TiO₂ nanowires 2 μ m and top view Figure 33 observations of the samples. Arrays of NWs 22-50nm in radius and lengths in the 0.5–2.0 μ m range were obtained.

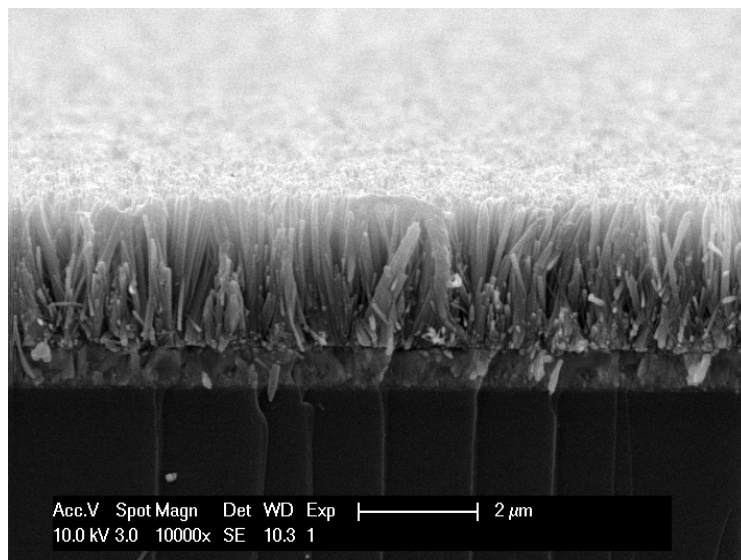


Figure 32. SEM cross section view for the 2 μ m TiO₂ nanowire

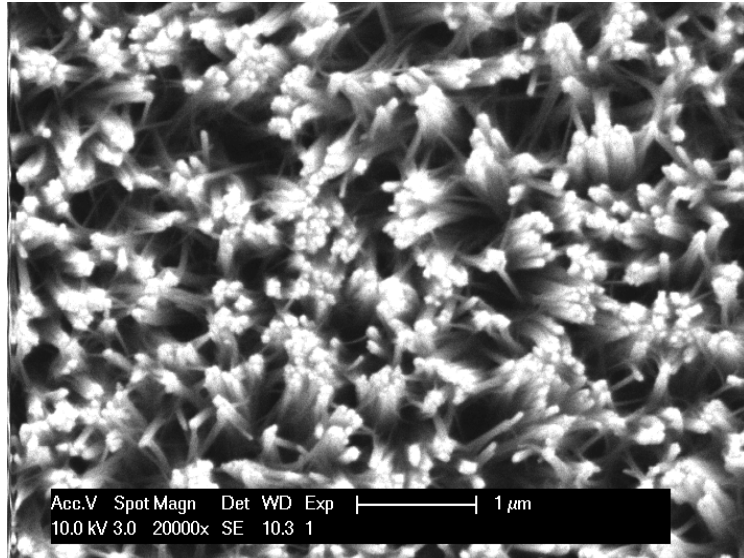


Figure 33. SEM top view for the 2 μm TiO₂ nanowire

5.0 CONCLUSION

This Master's Thesis research demonstrates the application of the electromagnetic computational technique FDTD for determining the light absorbance of a titania nanotube-array-based quantum dots solar cells, thereby providing information on how to optimize the nanowire-array dimensions for improved solar cell performance.

As discussed above, simulation results clearly demonstrate the advantage of using longer titania nanotube arrays of smaller pore size, which results in more surface area for quantum dots coating. However, the study can be extended to more complex situations where the angle-dependent effect is taken into account. The technique is a general one, and can also be used to simulate quantum dots solar cells fabricated using nanostructures of other geometries and materials as desired helping to guide experimental synthesis of nanostructured quantum dots solar cells. Simulation of nanowire arrays of significantly greater length is under currently working . This necessitates a substantial upgrade of our computational capabilities, which are not yet complete. However, next step would be focusing more on the angle-dependent factors.

REFERENCES

1. Dresselhaus, M. S.; Thomas, I. L. Alternative energy technologies. *Nature* 2001, *414*, 332-337.
2. Gur, N. A. Fromer, M. L. Geier and A. P. Alivisatos, *Science*, 2005, 310, 462–465.
3. P. Wang, S. M. Zakeeruddin, J. E. Moser, M. K. Nazeeruddin, T. Sekiguchi and M. Grätzel, *Nat. Mater.*, 2003, 2, 402–407.
4. Lewis, N. S.; Nocera, D. G. *Proc. Natl. Acad. Sci. U.S.A.* 2007, *104*, 20142–20152.
5. Fawer-Wasswer, M. Current status and outlook for photovoltaics and solar thermal power. *Sarasin Sustainable Investment Report*, 2004.
6. Green, M. A. *Sol. Energy* 2004, *76*, 3–8.
7. Alsema, E. A. *Prog. Photovoltaics* 2000, *8*, 17–25.
8. M. Pagliaro, G. Palmisano, R. Ciriminna and V. Loddo, *Energy Environ. Sci.*, 2009, *2*, 838–844.
9. A. Kongkanand, K. Tvrdy, K. Takechi, M. Kuno and P. V. Kamat, *J. Am. Chem. Soc.*, 2008, *130*, 4007–4015.
10. D. R. Baker and P. V. Kamat, *Adv. Funct. Mater.*, 2009, *19*, 805–811.
11. Yang, H. G.; Sun, C. H.; Qiao, S. Z.; Zou, J.; Liu, G.; Smith, S. C.; Cheng, H. M.; Lu, G. *Q. Nature* 2008, *453*, 638.
12. Jiu, J. T.; Isoda, S.; Wang, F. M.; Adachi, M. *J. Phys. Chem. B* 2006, *110*, 2087.

13. Khan, S. U. M.; Al-Shahry, M.; Ingler, W. B. *Science* 2002, 297, 2243.
14. Liu, B.; Aydil, E. S. *J. Am. Chem. Soc.* 2009, 131, 3985.
15. Zuruzi, A. S.; Kolmakov, A.; MacDonald, N. C.; Moskovits, M. *Appl. Phys. Lett.* 2006, 88, 102904.
16. Armstrong, A. R.; Armstrong, G.; Canales, J.; Garcia, R.; Bruce, P. G. *Adv. Mater.* 2005, 17, 862.
17. Ni, M.; Leung, M. K. H.; Leung, D. Y. C.; Sumathy, K. *Renew. Sust. Energ. Rev.* 2007, 11, 401.
18. Bach, U.; Lupo, D.; Comte, P.; Moser, J. E.; Weissortel, F.; Salbeck, J.; Spreitzer, H.; Gratzel, M. *Nature* 1998, 395, 583.
19. Law, M.; Greene, L. E.; Radenovic, A.; Kuykendall, T.; Liphardt, J.; Yang, P. D. *J. Phys. Chem. B* 2006, 110, 22652.
20. Greene, L. E.; Law, M.; Yuhas, B. D.; Yang, P. D. *J. Phys. Chem. C* 2007, 111, 18451.
21. Liu, J.; Kuo, Y. T.; Klabunde, K. J.; Rochford, C.; Wu, J.; Li, J. *ACS Appl. Mater. Interfaces* 2009, 1, 1645.
22. Burschka, J.; Pellet, N.; Moon, S. J.; Humphry-Baker, R.; Gao, P.; Nazeeruddin, M. K.; Gratzel, M. *Nature* 2013, 499, 316.
23. Ip, A. H.; Thon, S. M.; Hoogland, S.; Voznyy, O.; Zhitomirsky, D.; Debnath, R.; Levina, L.; Rollny, L. R.; Carey, G. H.; Fischer, A.; Kemp, K. W.; Kramer, I. J.; Ning, Z.; Labelle, A. J.; Chou, K. W.; Amassian, A.; Sargent, E. H. *Nat. Nanotechnol.* 2012, 7, 577.
24. Günes, S.; Neugebauer, H.; Sariciftci, N. S. *Chem. Rev.* 2007, 107, 1324. (20) Kim, J. Y.;
25. Kim, S. H.; Lee, H. H.; Lee, K.; Ma, W.; Gong, X.; Heeger, A. J. *Adv. Mater.* 2006, 18, 572.
26. Bavykin, D. V.; Friedrich, J. M.; Walsh, F. C. *Adv. Mater.* 2006, 18, 2807.
27. Hagfeldt, A.; Gratzel, M. *Chem. Rev.* 1995, 95, 49.
28. Burda, C.; Chen, X.; Narayanan, R.; El-Sayed, M. A. *Chem. Rev.* 2005, 105, 1025.

29. Murray, C. B.; Kagan, C. R.; Bawendi, M. G. *Annu. Rev. Mater.Sci.* 2000, 30, 545.
30. Cushing, B. L.; Kolesnichenko, V. L.; O'Connor, C. J. *Chem.Rev.* 2004, 104, 3893.
31. Linsebigler, A. L.; Lu, G. Q.; Yates, J. T. *Chem. Rev.* 1995, 95,735.
32. Chen, X.; Mao, S. S. *J. Nanosci. Nanotechnol.* 2006, 6, 906.
33. Roduner, E. *Chem. Soc. Rev.* 2006, 35, 583.
34. Valden, M.; Lai, X.; Goodman, D. W. *Science* 1998, 281, 1647.
35. Chen, X.; Mao, S. S. *Chem. Rev.* 2007, 107, 2891.
36. http://ecee.colorado.edu/~bart/book/book/chapter2/ch2_8.htm#fig2_8_3.
37. <http://pveducation.org/pvcdrom/pn-junction/absorption-coefficient>.
38. Dmitri V. Talapin, Jong-Soo Lee, Maksym V. Kovalenko. *Chemical Reviews*, 2010, Vol. 110, No. 1 427.
39. Banfield, J. F.; Veblen, D. R. *Am. Mineral.* 1992, 77, 545.
40. Cromer, D. T.; Herrington, K. J. *Am. Chem. Soc.* 1955, 77, 4708.
41. Marchand, R.; Brohan, L.; Tournoux, M. *Mater. Res. Bull.* 1980,15, 1129.
42. Xudong Wang, Zhaodong Li, Jian Shi, and Yanhao Yu. *Chem. Rev.* 2014, 114, 9346–9384.
43. Jun, Y.-w.; Choi, J.-s.; Cheon, J. *Angew. Chem., Int. Ed.* 2006, 45,3414.
44. Jun, Y.-w.; Lee, J.-H.; Choi, J.-s.; Cheon, J. *J. Phys. Chem. B* 2005,109, 14795.
45. Niederberger, M. *Acc. Chem. Res.* 2007, 40, 793.
46. Cozzoli, P. D.; Pellegrino, T.; Manna, L. *Chem. Soc. Rev.* 2006,35, 1195.
47. Ha, J. Y.; Sosnowchik, B. D.; Lin, L. W.; Kang, D. H.; Davydov, A. V. *Appl. Phys. Express* 2011, 4, 065002.

48. Lee, J. C.; Park, K. S.; Kim, T. G.; Choi, H. J.; Sung, Y. M. *Nanotechnology* 2006, 17, 4317.
49. Xiang, B.; Zhang, Y.; Wang, Z.; Luo, X. H.; Zhu, Y. W.; Zhang, H. Z.; Yu, D. P. *J. Phys. D: Appl. Phys.* 2005, 38, 1152.
50. Pradhan, S. K.; Reucroft, P. J.; Yang, F.; Dozier, A. J. *Cryst. Growth* 2003, 256, 83.
51. Wu, J.-M.; Shih, H. C.; Wu, W.-T. *Nanotechnology* 2006, 17, 105.
52. Penn, R. L.; Banfield, J. F. *Am. Mineral.* 1998, 83, 1077.
53. Barnard, A. S.; Zapol, P.; Curtiss, L. A. *J. Chem. Theory Comput.* 2005, 1, 107.
54. Oskam, G.; Nellore, A.; Penn, R. L.; Searson, P. C. *J. Phys. Chem. B* 2003, 107, 1734.
55. Shi, J.; Wang, X. *Energy Environ. Sci.* 2012, 5, 7918.
56. Penn, R. L.; Banfield, J. F. *Geochim. Cosmochim. Acta* 1999, 63, 1549.
57. Penn, R. L. *J. Phys. Chem. B* 2004, 108, 12707.
58. Ribeiro, C.; Lee, E. J. H.; Longo, E.; Leite, E. R. *ChemPhysChem* 2005, 6, 690.
59. Burrows, N. D.; Yuwono, V. M.; Penn, R. L. *MRS Bull.* 2010, 35, 133.
60. Ma, R.; Fukuda, K.; Sasaki, T.; Osada, M.; Bando, Y. *J. Phys. Chem. B* 2005, 109, 6210.
61. Amin, S. S.; Nicholls, A. W.; Xu, T. T. *Nanotechnology* 2007, 18, 445609.
62. Mukherjee, K.; Teng, T. H.; Jose, R.; Ramakrishna, S. *Appl. Phys. Lett.* 2009, 95, 012101.
63. Fujihara, K.; Kumar, A.; Jose, R.; Ramakrishna, S.; Uchida, S. *Nanotechnology* 2007, 18, 365709.
64. Kisumi, T.; Tsujiko, A.; Murakoshi, K.; Nakato, Y. *J. Electroanal. Chem.* 2003, 545, 99.
65. Albu, S. P.; Ghicov, A.; Macak, J. M.; Hahn, R.; Schmuki, P. *Nano Lett.* 2007, 7, 1286.
66. Zhu, Y.; Qian, Y. *Sci. China, Ser. G: Phys., Mech. Astron.* 2009, 52, 13.

67. Vayssieres, L. *Adv. Mater.* 2003, 15, 464.
68. Yu, H.; Buhro, W. E. *Adv. Mater.* 2003, 15, 416.
69. Chang, Y.; Lye, M. L.; Zeng, H. C. *Langmuir* 2005, 21, 3746.
70. Sun, Y.; Gates, B.; Mayers, B.; Xia, Y. *Nano Lett.* 2002, 2, 165.
71. Simon, C. J.; Dupuy, D. E.; Mayo-Smith, W. W. *Radiographics* 2005, 25 (Suppl 1), S69.
72. Jia, X.; He, W.; Zhang, X.; Zhao, H.; Li, Z.; Feng, Y. *Nanotechnology* 2007, 18, 075602.
73. Gedye, R.; Smith, F.; Westaway, K.; Ali, H.; Baldisera, L.; Laberge, L.; Rousell, J. *Tetrahedron Lett.* 1986, 27, 279.
74. Chen, Z.; Li, S.; Yan, Y. *Chem. Mater.* 2005, 17, 2262.
75. Cundy, C. S.; Cox, P. A. *Chem. Rev.* 2003, 103, 663.
76. Motuzas, J.; Julbe, A.; Noble, R. D.; Guizard, C.; Beresnevicius, Z. J.; Cot, D. *Microporous Mesoporous Mater.* 2005, 80, 73.
77. Baghbanzadeh, M.; Carbone, L.; Cozzoli, P. D.; Kappe, C. O. *Angew. Chem., Int. Ed. Engl.* 2011, 50, 11312.
78. Park, J.; Joo, J.; Kwon, S. G.; Jang, Y.; Hyeon, T. *Angew. Chem., Int. Ed. Engl.* 2007, 46, 4630.
79. Kwon, S. G.; Hyeon, T. *Acc. Chem. Res.* 2008, 41, 1696.
80. Bilecka, I.; Niederberger, M. *Nanoscale* 2010, 2, 1358.
81. Gressel-Michel, E.; Chaumont, D.; Stuerger, D. J. *Colloid Interface Sci.* 2005, 285, 674.
82. Wu, X.; Jiang, Q.-Z.; Ma, Z.-F.; Fu, M.; Shangguan, W.-F. *Solid State Commun.* 2005, 136, 513.
83. Ma, G.; Zhao, X.; Zhu, J. *Int. J. Mod. Phys. B* 2005, 19, 2763.
84. Yamamoto, T.; Wada, Y.; Yin, H.; Sakata, T.; Mori, H.; Yanagida, S. *Chem. Lett.* 2002, 964.

85. Szabó, D. V.; Vollath, D.; Arnold, W. *Ceram. Trans.* 2001, 111,217.
86. Ye, Z. Z.; Huang, J. Y.; Xu, W. Z.; Zhou, J.; Wang, Z. L. *Solid State Commun.* 2007, 141, 464.
87. Yang, M.; Ding, B.; Lee, S.; Lee, J.-K. *J. Phys. Chem. C* 2011, 115, 14534.
88. Ho, C.; Qiao, R.; Heng, J. B.; Chatterjee, A.; Timp, R. J.; Aluru, N. R.; Timp, G. *Proc. Natl. Acad. Sci. U.S.A.* **2005**, 102, 10445.
89. Vorotyntsev, M. A.; Badiali, J. P.; Vieil, E. *Electrochim. Acta* **1996**, 41, 1375.
90. Mathias, M. F.; Haas, O. *J. Phys. Chem.* **1992**, 96, 3174.
91. Buck, R. P.; Mundt, C. *Electrochim. Acta* **1999**, 44, 1999.
92. Van Soestbergen, M.; Biesheuvel, P. M.; Bazant, M. Z. *Phys. Rev. E: Stat., Nonlinear, Soft Matter Phys.* **2010**, 81, 021503.
93. Lai, W.; Haile, S. M. *Phys. Chem. Chem. Phys.* **2008**, 10, 865.
94. Batzill, M.; Diebold, U. *Prog. Surf. Sci.* **2005**, 79, 47.
95. Kim, J. R.; So, H. M.; Park, J. W.; Kim, J. J.; Kim, J.; Lee, C. J.; Lyu, S. C. *Appl. Phys. Lett.* **2002**, 80, 3548.
96. Tsong, T. T. *Surf. Sci.* **1979**, 81, 28.
97. Ishii, H.; Hayashi, N.; Ito, E.; Washizu, Y.; Sugi, K.; Kimura, Y.; Niwano, M.; Ouchi, Y.; Seki, K. *Phys. Status Solidi A* **2004**, 201,1075.
98. Nishi, T.; Kanai, K.; Ouchi, Y.; Willis, M. R.; Seki, K. *Chem. Phys.* **2006**, 325, 121.
99. Liu, G. M.; Schulmeyer, T.; Brotz, J.; Klein, A.; Jaegermann, W. *Thin Solid Films* **2003**, 431, 477.
100. Komolov, A.; Moller, P. J. *Colloids Surf., A* **2004**, 239, 49.
101. Prashant V. Kamat, Kevin Tvrdy, David R. Baker, and James G. Radich. *Chem. Rev.* **2010**, 110, 6664–6688

102. Sodergren, S.; Hagfeldt, A.; Olsson, J.; Lindquist, S. E. *J. Phys. Chem.* **1994**, *98*, 5552.
103. Cao, F.; Oskam, G.; Meyer, G. J.; Searson, P. C. *J. Phys. Chem.* **1996**, *100*, 17021.
104. Albery, W. J.; Bartlett, P. N. *J. Electrochem. Soc.* **1984**, *131*, 315.
105. Curran, J. S.; Lamouche, D. *J. Phys. Chem.* **1983**, *87*, 5405.
106. Grasso, C.; Nanu, M.; Goossens, A.; Burgelman, M. *Thin Solid Films* **2005**, *480*, 87.
107. Peter, L. M.; Duffy, N. W.; Wang, R. L.; Wijayantha, K. G. U. *J. Electroanal. Chem.* **2002**, *524*, 127.
108. Benkstein, K. D.; Kopidakis, N.; de Lagemaat, J. V.; Frank, A. J. In *Quantum Dots, Nanoparticles and Nanowires*; Guyot Sionnest, P., Mattoussi, H., Wang, Z. L., Eds.; Materials Research Society: Warrendale, PA, 2004; Vol. 789; pp 325.
109. Jennings, J. R.; Ghicov, A.; Peter, L. M.; Schmuki, P.; Walker, A. B. *J. Am. Chem. Soc.* **2008**, *130*, 13364.
110. Halme, J.; Boschloo, G.; Hagfeldt, A.; Lund, P. *J. Phys. Chem. C* **2008**, *112*, 5623.
111. Nelson, J.; Haque, S. A.; Klug, D. R.; Durrant, J. R. *Phys. Rev. B: Condens. Matter Mater. Phys.* **2001**, *63*, 205321.
112. Quintana, M.; Edvinsson, T.; Hagfeldt, A.; Boschloo, G. *J. Phys. Chem. C* **2007**, *111*, 1035.
113. Frank, A. J.; Kopidakis, N.; van de Lagemaat, J. *Coord. Chem. Rev.* **2004**, *248*, 1165.
114. Dloczik, L.; Ieperuma, O.; Lauermann, I.; Peter, L. M.; Ponomarev, E. A.; Redmond, G.; Shaw, N. J.; Uhlendorf, I. *J. Phys. Chem. B* **1997**, *101*, 10281.
115. van de Lagemaat, J.; Frank, A. J. *J. Phys. Chem. B* **2000**, *104*, 4292.
116. Bisquert, J.; Cahen, D.; Hodes, G.; Rühle, S.; Zaban, A. *J. Phys. Chem. B* **2004**, *108*, 8106.
117. Konenkamp, R. *Phys. Rev. B* **2000**, *61*, 11057.
118. Konenkamp, R.; Henninger, R.; Hoyer, P. *J. Phys. Chem.* **1993**, *97*, 7328.

119. Koenkamp, R.; Henninger, R. *Appl. Phys. A: Mater. Sci. Process.* **1994**, *58*, 87.
120. Peter, L. M.; Ponomarev, E. A.; Franco, G.; Shaw, N. J. *Electrochim. Acta* **1999**, *45*, 549.
121. Hoyer, P.; Koenkamp, R. *Appl. Phys. Lett.* **1995**, *66*, 349.
122. de Jongh, P. E.; Vanmaekelbergh, D. *Phys. Rev. Lett.* **1996**, *77*, 3427.
123. Fisher, A. C.; Peter, L. M.; Ponomarev, E. A.; Walker, A. B.; Wijyantha, K. G. U. *J. Phys. Chem. B* **2000**, *104*, 949.
124. de Jongh, P. E.; Vanmaekelbergh, D. *J. Phys. Chem. B* **1997**, *101*, 2716.
125. Vanmaekelbergh, D.; Marin, F. I.; vandeLagemaat, J. *Ber. Bunsen- Ges. Phys. Chem. Chem. Phys.* **1996**, *100*, 616.
126. Schwarzburg, K.; Willig, F. *Appl. Phys. Lett.* **1991**, *58*, 2520.
127. Petrozza, A.; Groves, C.; Snaith, H. J. *J. Am. Chem. Soc.* **2008**, *130*, 12912.
128. Amaldi, E.; Fermi, E. *Phys. Rev.* **1936**, *50*, 899.
129. Gonzalez-Vazquez, J. P.; Anta, J. A.; Bisquert, J. *J. Phys. Chem. C* **2010**, *114*, 8552.
130. Villanueva-Cab, J.; Wang, H.; Oskam, G.; Peter, L. M. *J. Phys. Chem. Lett.* **2010**, *1*, 748.
131. Peter, L. M.; Wijyantha, K. G. U. *Electrochem. Commun.* **1999**, *1*, 576.
132. Zhu, K.; Kopidakis, N.; Neale, N. R.; van de Lagemaat, J.; Frank, A. J. *J. Phys. Chem. B* **2006**, *110*, 25174.
133. Bisquert, J.; Vikhrenko, V. S. *J. Phys. Chem. B* **2004**, *108*, 2313.
134. Schmidlin, F. W. *Philos. Mag. B: Phys. Condens. Matter Stat. Mech. Electron. Opt. Magn. Prop.* **1980**, *41*, 535.
135. Peter, L. *Acc. Chem. Res.* **2009**, *42*, 1839.
136. Anta, J. A. *Energy Environ. Sci.* **2009**, *2*, 387.

137. Anta, J. A.; Mora-Sero, I.; Dittrich, T.; Bisquert, J. *Phys. Chem. Chem. Phys.* **2008**, *10*, 4478.
138. van de Lagemaat, J.; Zhu, K.; Benkstein, K. D.; Frank, A. J. *Inorg. Chim. Acta* **2008**, *361*, 620.
139. Graetzel, M. *Acc. Chem. Res.* **2009**, *42*, 1788.
140. Ofir, A.; Grinis, L.; Zaban, A. *J. Phys. Chem. C* **2008**, *112*, 2779.
141. Haque, S. A.; Palomares, E.; Cho, B. M.; Green, A. N. M.; Hirata, N.; Klug, D. R.; Durrant, J. R. *J. Am. Chem. Soc.* **2005**, *127*, 3456.
142. Gong, D.; Grimes, C. A.; Varghese, O. K.; Hu, W. C.; Singh, R. S.; Chen, Z.; Dickey, E. *C. J. Mater. Res.* **2001**, *16*, 3331.
143. Hoyer, P. *Langmuir* **1996**, *12*, 1411.
144. Wang, Y. Q.; Hu, G. Q.; Duan, X. F.; Sun, H. L.; Xue, Q. K. *Chem. Phys. Lett.* **2002**, *365*, 427.
145. Du, G. H.; Chen, Q.; Che, R. C.; Yuan, Z. Y.; Peng, L. M. *Appl. Phys. Lett.* **2001**, *79*, 3702.
146. Kasuga, T.; Hiramatsu, M.; Hoson, A.; Sekino, T.; Niihara, K. *Langmuir* **1998**, *14*, 3160.
147. Adachi, M.; Murata, Y.; Okada, I.; Yoshikawa, S. *J. Electrochem. Soc.* **2003**, *150*, G488.
148. Khan, S. U. M.; Sultana, T. *Sol. Energy Mater. Sol. Cells* **2003**, *76*, 211.
149. Law, M.; Greene, L. E.; Johnson, J. C.; Saykally, R.; Yang, P. *Nature Mater.* **2005**, *4*, 455.
150. Sander, M. S.; Cote, M. J.; Gu, W.; Kile, B. M.; Tripp, C. P. *Adv. Mater.* **2004**, *16*, 2052.
151. Mor, G. K.; Shankar, K.; Paulose, M.; Varghese, O. K.; Grimes, C. A. *Nano Lett.* **2006**, *6*, 215.
152. Aurora, P.; Rhee, P.; Thompson, L. *J. Electrochem. Soc.* **2010**, *157*, K152.
153. Zhu, K.; Neale, N. R.; Miedaner, A.; Frank, A. J. *Nano Lett.* **2007**, *7*, 69.

154. Baker, D. R.; Kamat, P. V. *Adv. Funct. Mater.* **2009**, *19*, 805.
155. Kuno, M. *Phys. Chem. Chem. Phys.* **2008**, *10*, 620.
156. Hochbaum, A. I.; Yang, P. D. *Chem. Rev.* **2010**, *110*, 527.
157. Zhu, K.; Neale, N. R.; Miedaner, A.; Frank, A. J. *Nano Lett.* **2007**, *7*, 69.
158. Hu, L.; Chen, G. *Nano Lett.* **2007**, *7*, 3249.
159. Zhu, K.; Vinzant, T. B.; Neale, N. R.; Frank, A. J. *Nano Lett.* **2007**, *7*, 3739.
160. Tian, Z. R. R.; Voigt, J. A.; Liu, J.; McKenzie, B.; McDermott, M. J.; Rodriguez, M. A.; Konishi, H.; Xu, H. F. *Nature Mater.* **2003**, *2*, 821.
161. Ohsaki, Y.; Masaki, N.; Kitamura, T.; Wada, Y.; Okamoto, T.; Sekino, T.; Niihara, K.; Yanagida, S. *Phys. Chem. Chem. Phys.* **2005**, *7*, 4157.
162. Archana, P. S.; Jose, R.; Vijila, C.; Ramakrishna, S. *J. Phys. Chem. C* **2009**, *113*, 21538.
163. Donegá, C. de M. *Chem. Soc. Rev.* **2011**, *40*, 1512.
164. Konstantatos, G.; Howard, I.; Fischer, A.; Hoogland, S.; Clifford, J.; Klem, E.; Levina, L.; Sargent, E. H. *Nature* **2006**, *442*, 180.
165. Clifford, J. P.; Konstantatos, G.; Johnston, K. W.; Hoogland, S.; Levina, L.; Sargent, E. H. *Nat. nanotechnol.* **2009**, *4*, 40.
166. Sun, L.; Choi, J. J.; Stachnik, D.; Bartnik, A. C.; Hyun, B.-R.; Malliaras, G. G.; Hanrath, T.; Wise, F. W. *Nat. Nanotechnol.* **2012**, *7*, 369.
167. Colvin, V. L.; Schlamp, M. C.; Alivisatos, A. P. *Nature* **1994**, *370*, 354.
168. Tessler, N.; Medvedev, V.; Kazes, M.; Kan, S.; Banin, U. *Science* **2002**, *295*, 1506.
169. Kwon, S. G.; Piao, Y.; Park, J.; Angappane, S.; Jo, Y.; Hwang, N. M.; Park, J. G.; Hyeon, T. *J. Am. Chem. Soc.* **2007**, *129*, 12571.
170. Shevchenko, E. V.; Talapin, D. V.; Schnablegger, H.; Kornowski, A.; Festin, O.; Svedlindh, P.; Haase, M.; Weller, H. *J. Am. Chem. Soc.* **2003**, *125*, 9090.

171. de Mello Donega, C.; Liljeroth, P.; Vanmaekelbergh, D. *Small* **2005**, *1*, 1152.
172. Talapin, D. V.; Rogach, A. L.; Kornowski, A.; Haase, M.; Weller, H. *Nano Lett.* **2001**, *1*, 207.
173. Yin, Y.; Alivisatos, A. P. *Nature* **2005**, *437*, 664.
174. Murray, C. B.; Kagan, C. R.; Bawendi, M. G. *Annu. Rev. Mater. Sci.* **2000**, *30*, 545.
175. *Monodispersed Nanoparticles*; Sugimoto, T., Ed.; Elsevier: New York, 2001.
176. Blackman, B.; Battaglia, D. M.; Mishima, T. D.; Johnson, M. B.; Peng, X. *Chem. Mater.* **2007**, *19*, 3815.
177. Peng, Z. A.; Peng, X. *J. Am. Chem. Soc.* **2002**, *124*, 3343.
178. Steigerwald, M. L.; Alivisatos, A. P.; Gibson, J. M.; Harris, T. D.; Kortan, R.; Muller, A. J.; Thayer, A. M.; Duncan, T. M.; Douglass, D. C.; Brus, L. E. *J. Am. Chem. Soc.* **1988**, *110*, 3046.
179. Morello, G.; De Giorgi, M.; Kudera, S.; Manna, L.; Cingolani, R.; Anni, M. *J. Phys. Chem. C* **2007**, *111*, 5846.
180. Yong, K.-T.; Sahoo, Y.; Swihart, M. T.; Prasad, P. N. *J. Phys. Chem. C* **2007**, *111*, 2447.
181. Micic, O. I.; Curtis, C. J.; Jones, K. M.; Sprague, J. R.; Nozik, A. J. *J. Phys. Chem.* **1994**, *98*, 4966.
182. Dimitrijevic, N. M.; Rajh, T.; Ahrenkiel, P.; Nedeljkovic, J. M.; Micic, O. I.; Nozik, A. J. *J. Phys. Chem. B* **2005**, *109*, 18243.
183. Talapin, D. V.; Rogach, A. L.; Shevchenko, E. V.; Kornowski, A.; Haase, M.; Weller, H. *J. Am. Chem. Soc.* **2002**, *124*, 5782.
184. Battaglia, D.; Peng, X. *Nano Lett.* **2002**, *2*, 1027.
185. Hines, M. A.; Scholes, G. D. *Adv. Mater.* **2003**, *15*, 1844.
186. Lin, W.; Fritz, K.; Guerin, G.; Bardajee, G. R.; Hinds, S.; Sukhovatkin, V.; Sargent, E. H.; Scholes, G. D.; Winnik, M. A. *Langmuir* **2008**, *24*, 8215.

187. Lee, S.-M.; Jun, Y.-W.; Cho, S.-N.; Cheon, J. *J. Am. Chem. Soc.* **2002**, *124*, 11244.
188. Cademartiri, L.; Bertolotti, J.; Sapienza, R.; Wiersma, D. S.; vonFreymann, G.; Ozin, J. *J. Phys. Chem. B* **2006**, *110*, 671.
189. Abel, K. A.; Shan, J. N.; Boyer, J. C.; Harris, F.; van Veggel, F. *Chem. Mater.* **2008**, *20*, 3794.
190. Urban, J. J.; Talapin, D. V.; Shevchenko, E. V.; Murray, C. B. *J. Am. Chem. Soc.* **2006**, *128*, 3248.
191. Peng, X.; Wickham, J.; Alivisatos, A. P. *J. Am. Chem. Soc.* **1998**, *120*, 5343.
192. Chen, Y.; Johnson, E.; Peng, X. *J. Am. Chem. Soc.* **2007**, *129*, 10937.
193. Talapin, D. V.; Rogach, A. L.; Haase, M.; Weller, H. *J. Phys. Chem. B* **2001**, *105*, 12278.
194. Reiss, P.; Bleuse, J.; Pron, A. *Nano Lett.* **2002**, *2*, 781.
195. Qu, L.; P., X. *J. Am. Chem. Soc.* **2002**, *124*, 2049.
196. Anikeeva, P. O.; Halpert, J. E.; Bawendi, A. G.; Bulovic', V. *NanoLett.* **2007**, *7*, 2196.
197. Peng, X.; Schlamp, M. C.; Kadavanich, A. V.; Alivisatos, A. P. *J. Am. Chem. Soc.* **1997**, *119*, 7019.
198. Wehrenberg, B. L.; Wang, C. J.; Guyot-Sionnest, P. *J. Phys. Chem. B* **2002**, *106*, 10634.
199. Vanmaekelbergh, D.; Liljeroth, P. *Chem. Soc. Rev.* **2005**, *34*, 299.
200. Chandler, R. E.; Houtepen, A. J.; Nelson, J.; Vanmaekelbergh, D. *Phys. Rev. B* **2007**, *75*, 085325.
201. Banin, U.; Cao, Y. W.; Katz, D.; Millo, O. *Nature* **1999**, *400*, 542.
202. S. Koc, *Czech. J. Phys.* **7** (1957) 91.
203. V.S. Vavilov, *J. Phys. Chem. Solids* **8** (1959) 223.
204. J. Tauc, *J. Phys. Chem. Solids* **8** (1959) 219.

205. V.N. Ivakhno, Sov. Phys. Solid State 14 (1972) 481.
206. A.J. Nozik / Chemical Physics Letters 457 (2008) 3–11.
207. O. Christensen, J. Appl. Phys. 47 (1976) 689.
208. A.R. Beattie, J. Phys. Chem. Solids 24 (1962) 1049.
209. Andras G. Pattantyus-Abraham, Illan J. Kramer. ACS NANO. VOL. 4 ▪ NO. 6 ▪ 3374–3380 -2010.
210. S. Kolodinski, J.H. Werner, T. Wittchen, H.J. Queisser, Appl. Phys. Lett. 63 (1993) 2405.
211. N.S. Baryshev, M.P. Shchetinin, S.P. Chashchin, Y.S. Kharionovskii, I.S. Aver'yanov, Sov. Phys. Semicond. 8 (1974) 192.
212. http://docs.lumerical.com/en/gain_quantum_dot_laser.html.
213. http://docs.lumerical.com/en/solvers_finite_difference_time_domain.html.